



# Optogenetic stimulation of the auditory pathway

Victor H. Hernandez,<sup>1,2</sup> Anna Gehrt,<sup>1</sup> Kirsten Reuter,<sup>1,2</sup> Zhizi Jing,<sup>1,3</sup> Marcus Jeschke,<sup>1</sup> Alejandro Mendoza Schulz,<sup>1</sup> Gerhard Hoch,<sup>1,2</sup> Matthias Bartels,<sup>4</sup> Gerhard Vogt,<sup>2,5</sup> Carolyn W. Garnham,<sup>2,5</sup> Hiromu Yawo,<sup>6</sup> Yugo Fukazawa,<sup>7</sup> George J. Augustine,<sup>8,9</sup> Ernst Bamberg,<sup>10</sup> Sebastian Kügler,<sup>11,12</sup> Tim Salditt,<sup>4,12</sup> Livia de Hoz,<sup>13</sup> Nicola Strenzke,<sup>3</sup> and Tobias Moser<sup>1,2,12</sup>

<sup>1</sup>InnerEarLab, Department of Otolaryngology, University Medical Center Göttingen, Göttingen, Germany. <sup>2</sup>Bernstein Focus for Neurotechnology, University of Göttingen, Göttingen, Germany. <sup>3</sup>Auditory Systems Physiology Group, Department of Otolaryngology, University Medical Center Göttingen, Göttingen, Germany. <sup>4</sup>Department of Physics, University of Göttingen, Göttingen, Germany. <sup>5</sup>MED-EL, Innsbruck, Austria and MED-EL Germany, Starnberg, Germany. <sup>6</sup>Molecular and Cellular Neuroscience Laboratory, Department of Developmental Biology and Neuroscience, Tohoku University Graduate School of Life Sciences, Sendai, Japan. <sup>7</sup>Department of Anatomy and Molecular and Cellular Biology, School of Medicine, Nagoya University, Nagoya, Japan. <sup>8</sup>Program in Neuroscience and Behavioral Disorders, Duke-NUS Graduate Medical School, Singapore. <sup>9</sup>Center for Functional Connectomics, Korea Institute of Science and Technology, Seoul, Republic of Korea. <sup>10</sup>Department of Biophysical Chemistry, Max Planck Institute of Biophysics, Frankfurt, Germany. <sup>11</sup>Department of Neurology, University Medical Center Göttingen, Göttingen, Germany. <sup>12</sup>Center for Nanoscale Microscopy and Molecular Physiology of the Brain, University of Göttingen, Göttingen, Germany. <sup>13</sup>Cognitive Neurophysiology Lab, Department of Neurogenetics, Max Planck Institute for Experimental Medicine, Göttingen, Germany.

**Auditory prostheses can partially restore speech comprehension when hearing fails. Sound coding with current prostheses is based on electrical stimulation of auditory neurons and has limited frequency resolution due to broad current spread within the cochlea. In contrast, optical stimulation can be spatially confined, which may improve frequency resolution. Here, we used animal models to characterize optogenetic stimulation, which is the optical stimulation of neurons genetically engineered to express the light-gated ion channel channelrhodopsin-2 (ChR2). Optogenetic stimulation of spiral ganglion neurons (SGNs) activated the auditory pathway, as demonstrated by recordings of single neuron and neuronal population responses. Furthermore, optogenetic stimulation of SGNs restored auditory activity in deaf mice. Approximation of the spatial spread of cochlear excitation by recording local field potentials (LFPs) in the inferior colliculus in response to suprathreshold optical, acoustic, and electrical stimuli indicated that optogenetic stimulation achieves better frequency resolution than monopolar electrical stimulation. Virus-mediated expression of a ChR2 variant with greater light sensitivity in SGNs reduced the amount of light required for responses and allowed neuronal spiking following stimulation up to 60 Hz. Our study demonstrates a strategy for optogenetic stimulation of the auditory pathway in rodents and lays the groundwork for future applications of cochlear optogenetics in auditory research and prosthetics.**

## Introduction

The electrical cochlear implant (CI) is considered the most successful neuroprosthesis. Implanted in more than 200,000 hearing-impaired subjects worldwide, CIs enable open speech comprehension in the majority of users (1–6). CIs also have become an important tool in auditory research (2), as they bypass the dysfunctional sensory organ of Corti in the cochlea via direct electrical stimulation of spiral ganglion neurons (SGNs). In cases in which the auditory nerve (AN) is dysfunctional or absent (e.g., after tumor surgery), electrical stimulation of the cochlear nucleus by auditory brainstem implants can be performed, although it less frequently achieves open speech comprehension (7).

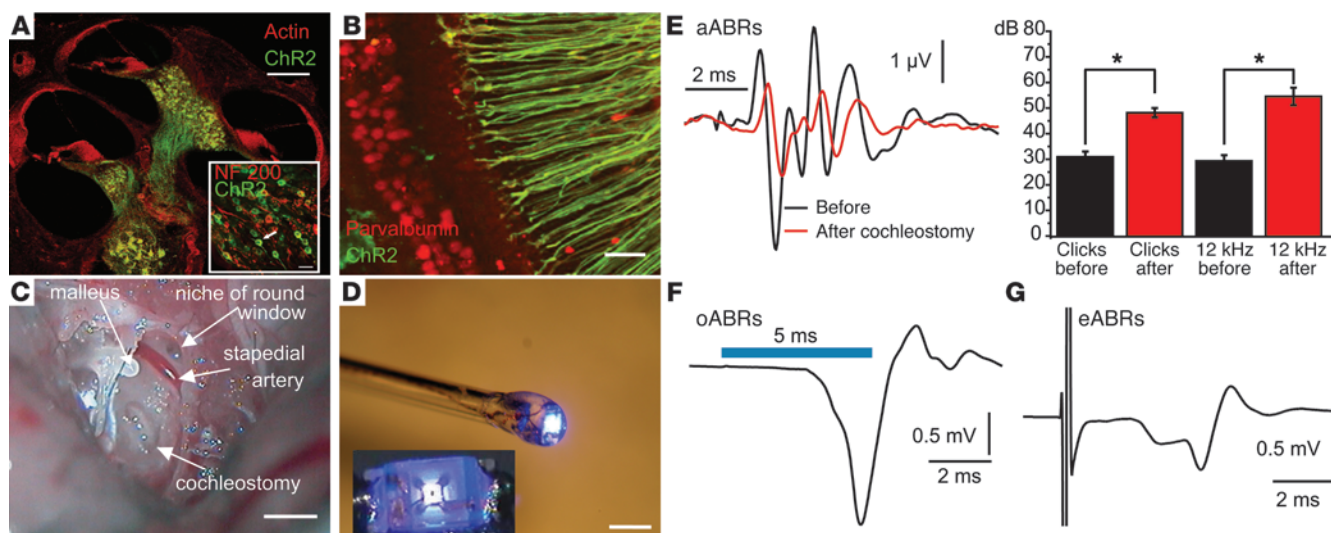
**Note regarding evaluation of this manuscript:** Manuscripts authored by scientists associated with Duke University, The University of North Carolina at Chapel Hill, Duke-NUS, and the Sanford-Burnham Medical Research Institute are handled not by members of the editorial board but rather by the science editors, who consult with selected external editors and reviewers.

**Authorship note:** Anna Gehrt, Kirsten Reuter, and Zhizi Jing contributed equally to this work.

**Conflict of interest:** Gerhard Vogt and Carolyn W. Garnham are employees of MED-EL, which also financially supported the study.

**Citation for this article:** *J Clin Invest*. 2014;124(3):1114–1129. doi:10.1172/JCI69050.

CIs and auditory brainstem implants are based on electrical sound coding. Electrical stimulation causes activation around the “tonotopic position” of a specific electrode contact in the cochlea or cochlear nucleus, respectively. CIs typically use 1–2 dozen electrode contacts, making limited use of the approximately 30,000 tonotopically ordered SGNs that ordinarily perform fine sampling of frequency-specific auditory information. The widespread electrical field around an electrode contact (8) leads to crosstalk (9) and further reduces the number of independent frequency channels (10, 11). Frequency resolution can be improved using multipolar stimulation at the expense of higher power consumption (12, 13) or intraneural stimulation (at least in animals) (14). Electrical coding is also limited for sound intensity, with an output dynamic range typically below 20 dB (5, 15). Thus, enhancing the frequency and intensity resolution of sound coding by auditory prostheses is a key objective for improving hearing restoration. Spatially confined activation of auditory neurons by light promises increased frequency resolution. Indeed, recent animal experiments have indicated excellent frequency resolution of cochlear stimulation with infrared light (16–18). However, the energy requirement for infrared stimulation (15  $\mu$ J per pulse for intracochlear stimulation; ref. 18) greatly exceeds that of monopolar electrical CIs (0.2  $\mu$ J per pulse; ref. 19), limiting the practical utility of optical strategies for prosthetic hearing restoration.

**Figure 1**

Optical activation of the auditory pathway in *ChR2* transgenic mice. (A) *ChR2*-YFP expression in SGNs in a section of an entire mouse cochlea following GFP immunolabeling and phalloidin-AF-568 labeling of actin. Scale bar: 500  $\mu$ m. Inset: SGNs costained for NF200 and GFP, arrow points to a GFP-positive SGN with typical bipolar morphology. Scale bar: 20  $\mu$ m. (B) *ChR2*-YFP is expressed in peripheral neurites of SGNs projecting to IHCs (radial fibers); immunolabeling for GFP and parvalbumin (outer hair cells and inner hair cells not included in this projection of confocal sections). Scale bar: 20  $\mu$ m. (C) typical surgical situs used for optical stimulation; retroauricular approach through the middle ear to the cochlea; cochleostomy and landmarks. Scale bar: 1 mm. (D)  $\mu$ LED probe. Using a micromanipulator, a glass capillary was used to position the  $\mu$ LED onto the cochleostomy. Scale bar: 1 mm. Inset shows en face view of the illuminated 200- $\mu$ m LED emitting surface. (E) aABRs before (black) and after (red) cochleostomy. Left panel: grand average of responses to 1,000 clicks at 80 dB SPL (peak equivalent), applied at 10 Hz. Right panel: aABR threshold for clicks and 12-kHz tone bursts ( $n = 11$  for both panels;  $*P < 0.001$ , paired Student's  $t$  test). (F) Representative oABRs in response to rectangular 5-ms power LED stimulation at 4 mW/mm<sup>2</sup> and 1 Hz (average of 56 trials). (G) Representative eABRs in response to stimulation with 900- $\mu$ A currents at 20 Hz via glass-insulated tungsten electrodes (one placed inside and one outside the cochlea; average of 200 trials).

Here, we used microbial light-gated channelrhodopsin-2 (*ChR2*) (20) to render SGNs sensitive to light. *ChR2* is a biophysically (20–23) and structurally (24) well-characterized cation channel (passive conductor) with low conductance (20). The generation and experimental application of *ChR2* variants with different properties has revolutionized the life sciences (“optogenetics,” reviewed in refs. 25, 26) and generated new avenues for medical therapies such as those aimed at restoring vision (27–30). In the present study, we explored the feasibility of optogenetic stimulation of auditory neurons in rodents. We used transgenic mice (31, 32) and rats (29) expressing *ChR2* under the *Thy1.2* promoter in auditory neurons and the adeno-associated virus-mediated (AAV-mediated) *ChR2* variant CatCh (33) in SGNs. We demonstrate optogenetic activation of SGNs (cochlear optogenetics) by optically evoked auditory brainstem responses (oABRs), the interaction of optogenetic and acoustic SGN stimulation, light-evoked single SGN activity, and local field potentials (LFPs) recorded in the inferior colliculus (IC). Using IC recordings, we indicate improved frequency resolution with optogenetic stimulation compared with that achieved with monopolar electrical stimulation, a finding that promises numerous opportunities for auditory research and future advances in hearing restoration with CIs.

## Results

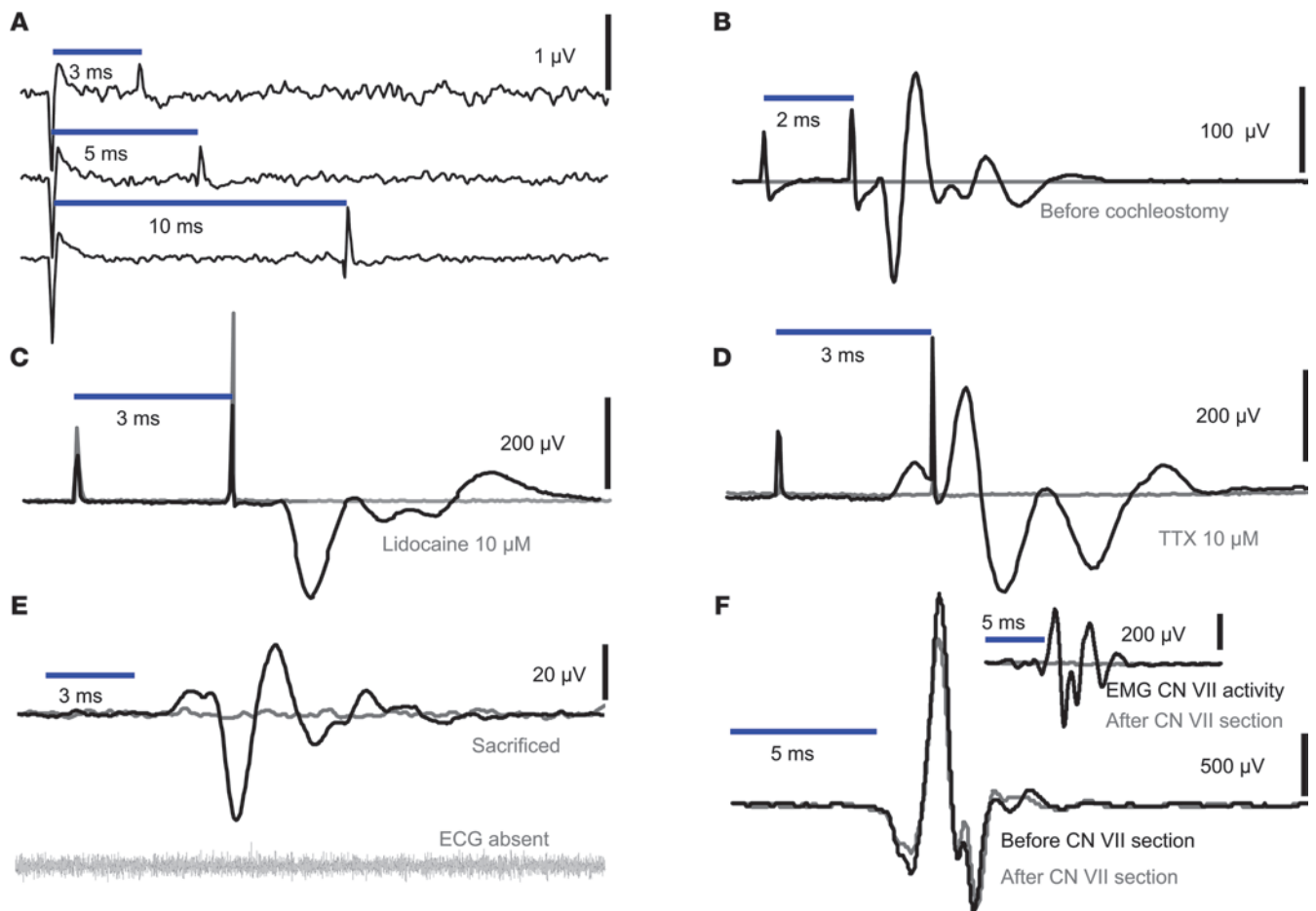
**Optogenetic stimulation of the auditory nerve.** Transgenic mice (32) expressed *ChR2*-YFP in the somata (Figure 1A and inset) as well as in the peripheral (Figure 1B) and central axons (Figure 1A) of almost

all SGNs. Within the cochlea, *ChR2* expression was restricted to SGNs, such that optogenetically evoked auditory activity can be safely attributed to SGNs and not hair cell stimulation (Figure 1B).

We established cochlear optogenetics in 4- to 20-week-old *ChR2* mice using light-emitting diodes (LEDs) (Figure 1D) or fiber-coupled lasers for different blue light stimulation strategies. Using a retroauricular approach to the middle ear, we either opened a small window in the cochlear capsule (transcochlear stimulation, cochleostomy diameter of 1 mm; Figure 1C and see Methods), or inserted the light emitter into the scala tympani via the round window (intracochlear stimulation). We first tested the activation of the auditory pathway by acoustic, optogenetic, and electrical stimulation using scalp recordings of neuronal population responses (ABRs: mean difference potential between a vertex and a mastoid needle electrode relative to ground, acoustic ABRs [aABRs]: averaging 1,000 trials, oABRs and electrical ABRs [eABRs]: averaging 100 trials, respectively). Due to the middle ear surgery and cochleostomy, the aABRs were mildly compromised (Figure 1E), as illustrated by the reduced amplitudes of the suprathreshold aABR and an elevation of the auditory threshold (20–30 dB,  $n = 11$ ,  $P < 0.001$  by a paired Student's  $t$  test). oABRs (Figure 1F) differed from aABRs (evoked by 80 dB clicks) in waveform, number of waves, and amplitude and were more comparable to eABRs (Figure 1G, Supplemental Figure 2, and ref. 34; supplemental material available online with this article; doi:10.1172/JCI69050DS1). This may reflect the recruitment of more SGNs and a higher synchrony of firing (see below) induced by optogenetic versus acoustic stimu-



## technical advance

**Figure 2**

Specificity of oABRs for ChR2-mediated activation of the auditory pathway. (A) No oABRs upon projection of light onto the cochleostomy of a wild-type mouse. (B) No oABRs upon projection of light onto the cochlea prior to cochleostomy of a *ChR2* transgenic mouse (stimulus artifacts are absent because of careful positioning of the cables connected to the needle electrodes) and oABRs present after cochleostomy. (C and D) oABRs before and after placing a mini-gelfoam containing the sodium channel blocker lidocaine (C, 20 minutes of gelfoam application) or TTX (D, 63 minutes of gelfoam application) onto the cochleostomy. (E) Loss of oABRs evoked by projection of light onto the cochleostomy (*ChR2* mouse) after sacrificing with an overdose of ketamine (as evident from zero-line ECG). (F) oABRs of a *ChR2* mouse before and after severing the facial nerve (CN VII). Inset shows the light-evoked facial electromyogram (EMG), before and after dissecting the nerve. Stimulus: blue light power LED; 4 mW/mm<sup>2</sup> at the indicated duration at 1 Hz; 50 trials for all panels.

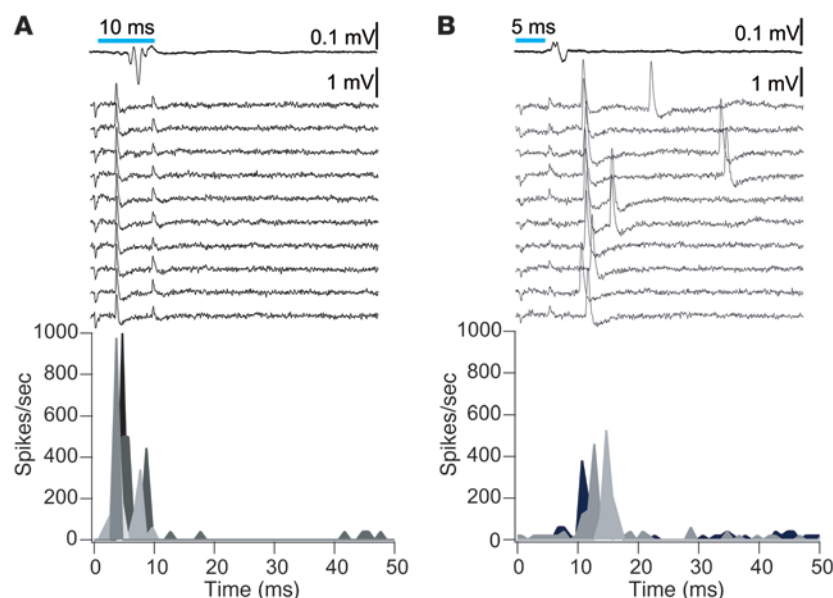
lation. oABRs could be obtained by all optical stimulation protocols (responses to intracochlear  $\mu$ LED implant or optical fiber in *ChR2* mice shown in Supplemental Figures 1 and 2). Moreover, oABRs were successfully elicited by transcochlear stimulation in *ChR2* transgenic rats, which showed expression of ChR2-Venus throughout the spiral ganglion (Supplemental Figure 6).

The oABRs appeared specific for ChR2-mediated activation of SGNs. We did not detect oABRs in response to 4 mW/mm<sup>2</sup> transcochlear irradiance in (a) wild-type mice (Figure 2A) or in *ChR2* mice when (b) light was projected onto their intact cochlea (Figure 2B); (c) SGN action potential generation was inhibited by applying the sodium channel blocker lidocaine (Figure 2C) or tetrodotoxin (TTX) (Figure 2D) to the cochleostomy; or (d) when mice had been sacrificed (Figure 2E). Moreover, oABRs to transcochlear LED stimulation persisted after severing the facial nerve (Figure 2F). We found that oABRs differed between animals in amplitude (e.g., Figure 2) and shape, but were reproducible within the same recording

(Supplemental Figure 10). We attribute this heterogeneity to differences in the size and position of the cochleostomy, the position and orientation of the LED lens assembly, the position of the electrode, and in the expression of ChR2 in SGNs.

Next, we studied optogenetic activation of single SGNs (Figure 3A) and consecutive propagation of the signal to neurons of the cochlear nucleus (Figure 3B) in *ChR2* mice. For this purpose, we established laser stimulation of the left cochlea via a 250- $\mu$ m plastic optical fiber placed onto a small cochleostomy. After confirming efficient optogenetic stimulation by recording oABRs, we drove a glass microelectrode toward the internal auditory canal, where the SGNs enter the cochlear nucleus with a penetration depth of at least 1,000  $\mu$ m. At high illumination intensities (22 mW), we observed optogenetically driven single-neuron spiking activity in nine neurons in three successful experiments, whereas an additional twenty-seven neurons showed spontaneous firing, but no light-evoked responses. In responsive neurons, each light pulse



**Figure 3**

Microelectrode recordings from individual neurons of the auditory pathway reveal activation by cochlear optogenetics. (A) Relatively short latencies and remarkably high reliability and temporal precision of single-neuron spiking near the internal auditory canal, presumably representing SGNs in response to intracochlear laser light stimulation. Simultaneously recorded oABRs are shown above the associated single-neuron traces. Bottom panel: poststimulus time histograms of several neurons, distinguished by grayscale values. (B) Single neuron responses encountered within the posterior part of the cochlear nucleus, showing slightly longer latencies, lower reliability, and increased jitter, likely representing principal neurons. Upper panels: average corresponding oABR and individual trials with responses of a single neuron. Bottom panel: PSTH of putative principal neurons of the cochlear nucleus. PSTH, peristimulus time histogram.

typically evoked one or two action potential(s), and only two neurons showed multiple spikes. Failures were observed in only three neurons, which showed additional spontaneous spiking. Six neurons showed short first spike latencies ( $4.8 \pm 0.3$  ms from light onset, and  $4.6 \pm 0.3$  ms when excluding one neuron with spontaneous firing), which we suggest represent SGNs. We found a very low trial-to-trial variance of the first spike timing ( $0.08 \pm 0.06$  ms<sup>2</sup> without versus  $0.40 \pm 0.03$  ms<sup>2</sup> with inclusion of the spontaneously active neuron). For a comparison, we report the SGN responses to brief acoustic (click) stimuli, which showed an average first spike latency of  $3.2 \pm 0.9$  ms ( $P < 0.01$  for comparison with optogenetic stimulation), with a mean trial-to-trial variance of  $0.7 \pm 1.0$  ms<sup>2</sup> ( $P < 0.02$  for comparison with optogenetic stimulation, when including the Chr2 SGNs with spontaneous firing) in a different set of experiments in wild-type C57Bl/6 mice. Three other neurons had a longer ( $13.2 \pm 1.6$  ms) and more variable ( $2.4 \pm 0.9$  ms<sup>2</sup>) optogenetically driven first spike latency and likely represent cochlear nucleus neurons. In summary, these findings demonstrate that cochlear optogenetics activates the auditory pathway.

**Cochlear optogenetics: masking of acoustic response and spread of cochlear excitation.** We studied whether depolarization of SGNs due to Chr2 activation would render them refractory to sound-evoked synaptic transmission from inner hair cells (IHCs). Such “light-on-tone” masking (17) would further corroborate the activation of the ascending auditory pathway by cochlear optogenetics and could provide a first estimate of the spread of light-evoked cochlear excitation. Following deafening of the contralateral ear (see Methods) of Chr2 mice, we performed a cochleostomy and positioned the  $\mu$ LED using oABRs as a reporter for efficient optogenetic stimulation. We then recorded aABRs in the absence and presence of the optogenetic masker. To enable safe detection of aABRs in spite of the large difference in oABR and aABR amplitudes (Figure 1), we started the optical stimulus 20 ms prior to the tone burst (Figure 4A). We maintained the optogenetic stimulation for a total of 40 ms and used an irradiance of 4 mW/mm<sup>2</sup> in order to achieve sufficiently sustained depolarization of SGNs despite partial Chr2 inactivation (Figure 8 and ref. 20). aABRs were masked by optogenetic stimulation of SGNs in a frequency-

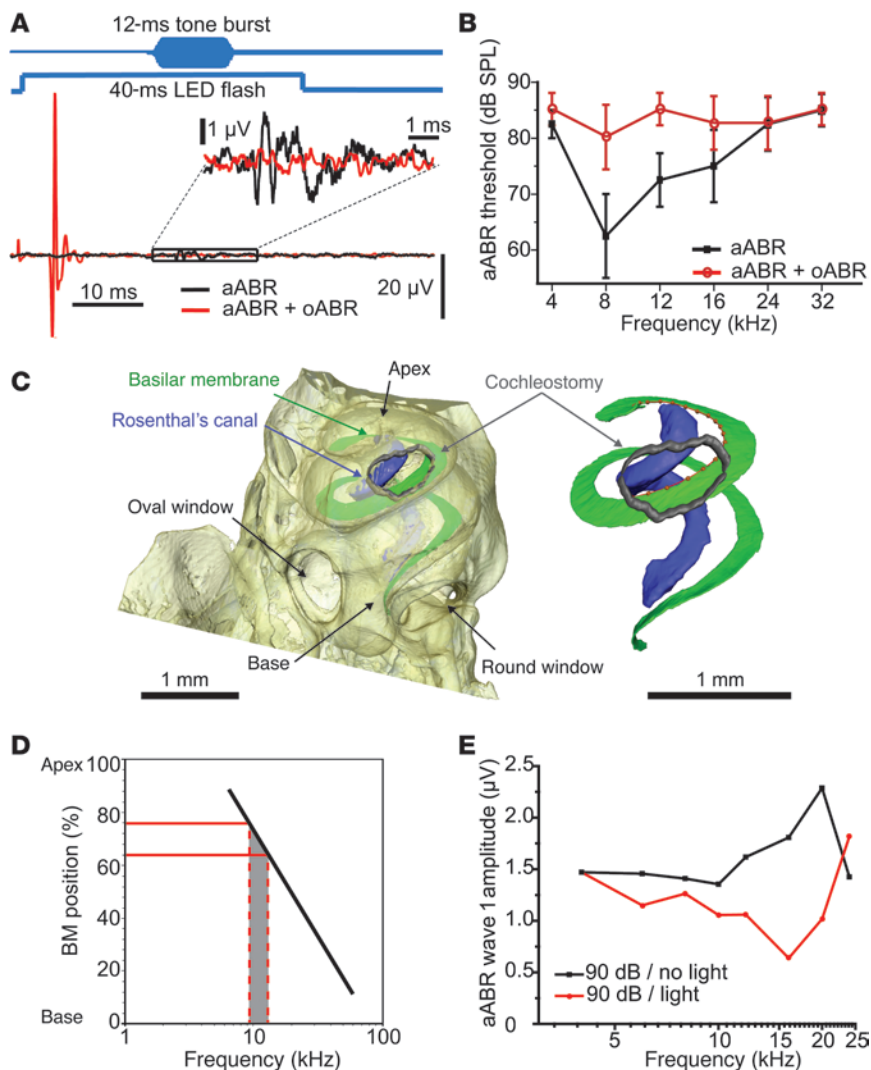
dependent manner: higher sound pressure levels were required to evoke detectable aABRs at 8 and 12 kHz ( $n = 4$ ;  $P < 0.05$ ; paired Student's  $t$  test; Figure 4B), but not at 4 or 16–32 kHz ( $P > 0.05$ ; paired Student's  $t$  test). However, optogenetic stimulation did not fully abolish the aABRs, which could, in principle, reflect the contribution of an incompletely deafened contralateral ear, low or absent Chr2 expression in a subset of SGNs (absent or incomplete depolarization block by Chr2 activation), or a broader spread of excitation of the acoustic versus the optogenetic response.

The frequency range at which we observed light masking of aABRs coincided with the tonotopic position of the cochleostomy, as identified by high-resolution x-ray phase-contrast tomography (ref. 35, Figure 4C, Supplemental Figure 8, and Supplemental Video 1). Resolution and contrast sufficed for tracing the basilar membrane (Figure 4C, inset). The frequency range embraced by a typical cochleostomy was estimated to be 8–12 kHz (Figure 4D), based on a previously established frequency map of the mouse cochlea (36). We interpret these findings to indicate that our transcochlear  $\mu$ LED illumination indeed affected sound coding by SGNs and that this effect was restricted to a tonotopic range of less than an octave. We note that this underestimates the potential frequency selectivity of optogenetic stimulation, because the  $\mu$ LED, a wide-angle surface emitter, was positioned roughly 1,200  $\mu$ m away from the SGNs (the sum of the distance from the  $\mu$ LED surface to the cochleostomy was 700  $\mu$ m and the distance from the cochleostomy to the radial fibers was 500  $\mu$ m), and no focusing of the light was used. “Light-on-tone” masking was also observed for suprathreshold aABRs in a different set of experiments ( $n = 10$ ). We analyzed the amplitude of aABR wave 1 and found an almost 3-fold maximal reduction following light stimulation (Figure 4E).

Next, we assessed the cochlear spread of excitation using multi-electrode array recordings of LFPs from the central nucleus of the IC (ICC), which provides access to tonotopically ordered input of the auditory pathway (refs. 37, 38, and Supplemental Figures 3 and 4). We inserted a 250- $\mu$ m optical fiber through the round window approximately 700  $\mu$ m into the scala tympani to stimulate the cochlear base SGNs (Figure 5 and Supplemental Figures 2 and 4). This approach is predicted to stimulate SGN sig-



## technical advance

**Figure 4**

Interaction of optogenetic and acoustic cochlear stimulation. **(A)** Following careful cochleostomy and positioning of a  $\mu$ LED, regular and light-masked acoustic thresholds were estimated by application of tone bursts of varying sound pressure levels (SPLs) and frequencies in the absence of optical stimulation (black) or following the cessation of an oABR that occurred at the onset of a concomitant 40-ms light stimulation (red). **(B)** Average aABR audiogram of four cochleostomized mice (best threshold not exceeding 70 dB) in the absence (black) and presence (red) of concomitant light; threshold increase upon light indicates masking due to a preceding optogenetic stimulation of the same population of neurons. **(C)** Tomography of an explanted mouse cochlea based on cone-beam in-line phase contrast at a compact laboratory x-ray source and a fast phase reconstruction procedure. Bony structures were segmented automatically; the basilar membrane (green), Rosenthal's canal (blue), and cochleostomy (gray) were traced with semiautomatic segmentation. A spline curve was fitted to the basilar membrane and was used to identify the position of the cochleostomy relative to the tonotopic map of the cochlea (**D**, modified from ref. 36). See Methods for further description. **(E)** Light-on-tone masking assessed as the change in P1–N1 aABR amplitude with simultaneous  $\mu$ LED stimulation.

naling at the frequency range around 55 kHz (36). No responses in this range were observed due to age-related hearing loss (39, 40) in the mouse strain (C57Bl/6 background) used in this study (Supplemental Figures 4 and 5). In parallel experiments, we used acoustic and monopolar electrical stimulation to compare the cochlear spread of excitation between the three modalities. The stimulus intensities were chosen as being suprathreshold for each modality, as judged by LFPs in the IC (Figure 5, B–D) and simultaneously measured ABRs (Supplemental Figure 2). We chose suprathreshold stimulation with the rationale that spatial selectivity of these intensities matters for the coding of many behaviorally relevant acoustic signals. Figure 5 illustrates the situs of the recording using a single-shank multielectrode array inserted into the ICC (Figure 5A) and provides representative LFP recordings from the 16 electrode contacts of the array showing spatiotemporal response patterns for the three different stimulus modes as a function of depth (Figure 5, B–D; see Supplemental Figure 3 for histological verification and LFPs). Responses to tone bursts (30 ms) of varying frequencies were used to map the tonotopic range of cochlear excitation in the IC (Supplemental Figure 4). We used frequency gradients along linear, multielectrode arrays to

calibrate the location of the responses to the electrical and optical stimulation within the tonotopic map of the ICC (38). While a comparison of spread of excitation in the cochlear base was feasible for optical and electrical stimulation, it was not feasible for acoustic stimulation due to the high-frequency hearing loss in most of the animals (Supplemental Figures 4 and 5). Instead, we compared the responses to optical and electrical stimulation with those evoked by a 31-kHz tone burst (80 dB, 30 ms) (Figure 5C).

Optogenetic responses (24 mW, 6 ms) (Figure 5B) showed spatial tuning similar to that of acoustic responses, whereby the maximum response was observed most ventrally in the IC (Figure 5I), as one would expect with stimulation of the high-frequency cochlear base. We found that responses to electrical stimulation (biphasic pulses, 250  $\mu$ A pulses of 80  $\mu$ s phase duration, 20  $\mu$ s interphase gap) (Figure 5D) were spatially more extended. Based on the spatial profile of LFPs, we calculated current source densities (CSDs) (Figure 5, E–H, and Supplemental Figure 4) for a first assessment of the cochlear spread of excitation based on IC activity (Figure 5E), as these allow better localization and more direct observation of the spatiotemporal distribution of the evoked transmembrane currents (41–43). In general, CSD analysis is thought to reflect the excitatory inputs onto

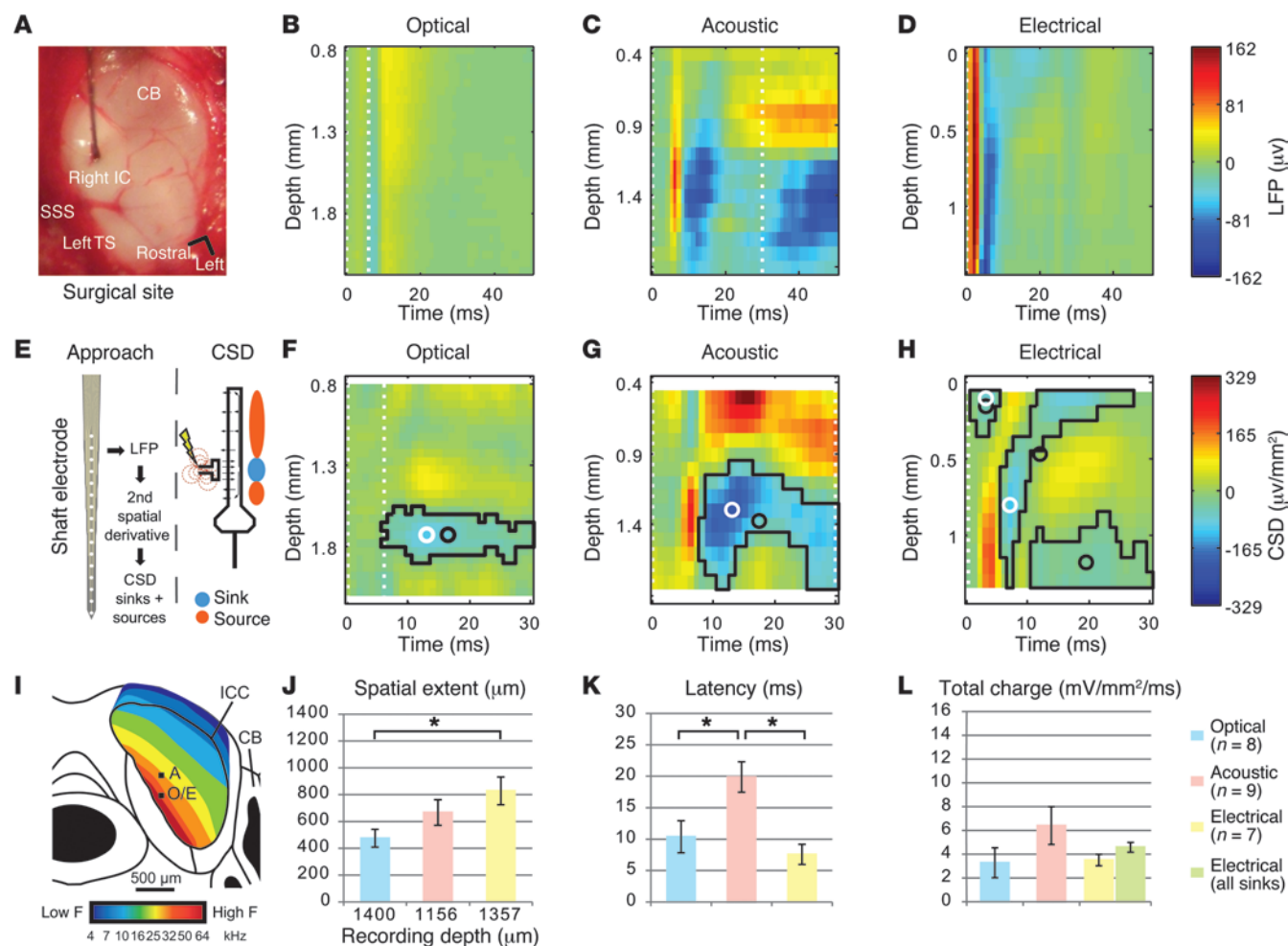


**Figure 5**

Assessment of the spread of cochlear excitation during optogenetic, acoustic, and electrical stimulation with multielectrode array recordings in the IC. (A) Surgical site with recording electrode inserted into the right ICC. SSS, superior sagittal sinus; TS, transverse sinus; CB, cerebellum. (B–D) False color-coded representative profiles of LFPs evoked by optical (B), acoustic (C), and electrical (D) stimulation, recorded with multielectrode arrays. Note that the absolute depth (ordinate) differs between B–D, because maximum responses were found in different IC layers. Dashed lines indicate stimulus duration. (E) Profiles of LFPs were transformed into CSD patterns via the second spatial derivative (42). (F–H) Illustrative CSD patterns after optical, acoustic, and electrical stimulation, respectively. Sinks are plotted in blue and sources in red. Significant sinks are outlined in black, with centroid and peak highlighted by black and white open circles. Note that multiple sinks were usually identified for electrical stimulation. (I) Schematic representation of the tonotopic map of a mouse IC (modified from ref. 37). Average recording depth (black squares) at which the sinks were identified was plotted at estimated electrode positions. A, acoustic; O, optical; E, electrical stimulation. (J–L) Characterization of sinks for the three different stimulation modalities. If several sinks were found, the sink with the largest total charge was used for further analysis. (J) Maximum spatial extents and recording depth at which the sink was found. (K) Peak latencies. (L) Total carried charge. The green bar indicates the charge carried by all sinks.

a population of neurons as current sinks and passive return currents as sources (42, 44). Consequently, we quantified the spatial extent of the major current sink along the tonotopic axis of the IC for all three modalities as a measure of cochlear spread of excitation (Figure 5, F–H). We found a significant difference in the spread of excitation between the stimulation modalities (Figure 5J, ANOVA:  $P < 0.05$ ). Under these conditions, we found that the spread of excitation for optogenetic stimulation ( $475 \pm 65.5 \mu\text{m}$ ) was at least as narrow as that for acoustic stimulation ( $666.7 \pm 95.7 \mu\text{m}$ ,  $p_{\text{optical-acoustic}} = \text{NS}$ ), while, as expected, monopolar electrical stimulation showed a broader spread ( $828.6 \pm 101.7 \mu\text{m}$ ,  $p_{\text{electrical-optogenetic}} < 0.05$ ). This finding qualitatively agrees with a recent study of infrared optical

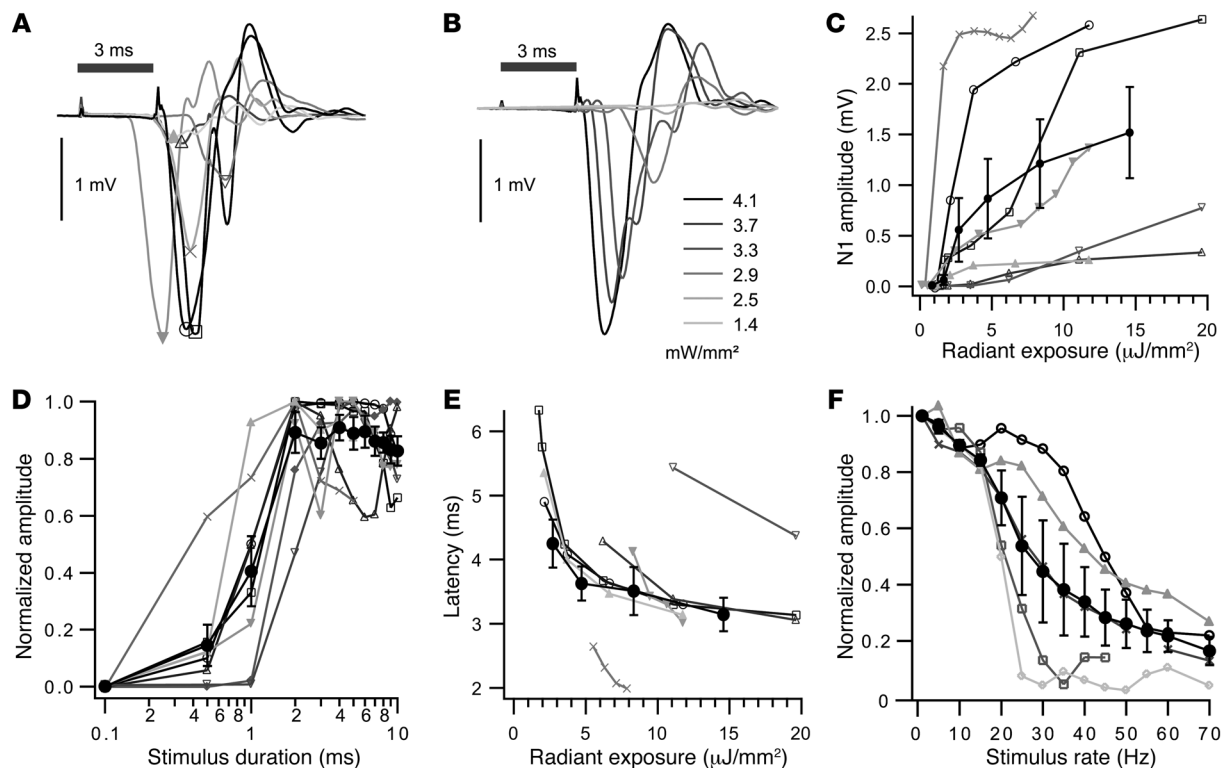
stimulation (18). We note that the spread of excitation after acoustic stimulation with higher stimulus frequencies in mice with high-frequency hearing is likely to be narrower than that seen at 31 kHz (45–47). Sink peak latencies were shorter with optogenetic and electrical stimulation than with tone bursts (Figure 5K; ANOVA,  $P < 0.01$ ;  $p_{\text{optical-electrical}} = \text{NS}$ ,  $p_{\text{optical-acoustic}} < 0.05$ ,  $p_{\text{electrical-acoustic}} < 0.01$ ). The total transferred charge was similar for all stimulus modalities (Figure 5L; ANOVA,  $P = 0.33$ ), indicating comparable levels of stimulation of the auditory pathway.

Since future optogenetic stimulation will likely rely on linear intracochlear arrays of light emitters, we performed x-ray tomographic measurements of the cochlear anatomy in mouse and rat





## technical advance

**Figure 6**

Effects of stimulus properties on oABRs. **(A)** oABRs of 8 mice elicited by focusing the light of an external power LED (5 ms, 4 mW/mm<sup>2</sup> at 1 or 5 Hz) onto the cochleostomy. Symbols indicate N1. Gray line values identify the same mice across **A** and **C–E**, and symbols additionally aid the identification of mice throughout **C–F**. **(B)** oABR stimulation of increasing irradiance (3-ms pulse duration at 1 Hz) of an exemplary mouse. **(C)** Increase of N1 amplitude with radiant exposure (irradiance as in **B**; pulse duration of 2, 3, or 5 ms at 1 Hz). Group average is indicated by black filled circles. **(D)** Increase in N1 amplitude (normalized for maximum amplitude) with stimulus duration. **(E)** Latency of oABRs (defined as N1 passing through 0.1 mV) as a function of irradiance. Group average is indicated by black filled circles. **(F)** Decrease in N1 amplitude (normalized for maximum amplitude) with stimulus rate (black filled circles indicate group average).

(Supplemental Figure 8 and Supplemental Video 1). Supplemental Figure 8 displays the size of the scala tympani as a function of the distance from the cochlear base, indicating the space available for an intracochlear implant. Using the anatomical information obtained from x-ray tomography, we performed theoretical studies of the spatial illumination profile elicited from a 50- $\mu$ m-sized blue LED (Lambertian emitter) facing the medial wall of the mouse cochlea (Supplemental Figure 9). For an upper estimate of the cochlear spread of excitation, we directed the  $\mu$ LED beam in the scala media toward the SGN somata in Rosenthal's canal rather than toward the peripheral neurites that project to the organ of Corti (favorable for energy requirement and frequency resolution). The full width at half-maximum of the light beam in the middle of the ganglion amounted to 250  $\mu$ m, which corresponds to 500  $\mu$ m at the basilar membrane and indicates excitation of roughly one-third of an octave by a single  $\mu$ LED. We note that neither collimation nor focusing of the light was implemented, which could help to further limit the spread of excitation in future devices. In summary, our results indicate an interaction of optogenetic and acoustic stimulation at the population response level and a reduced spread of cochlear excitation compared with that of electrical stimulation.

*Characterizing the stimulus dependence of oABRs.* Using transcochlear power LED stimulation, we characterized the effects of stimulus intensity (irradiance or radiant exposure), duration, and rate on

oABRs. Figure 6A shows the suprathreshold oABRs (average of 50 trials) of 8 mice and demonstrates large interindividual differences in latency, amplitude, and waveform. We attribute this heterogeneity between the animals to differences in the size and position of the cochleostomy, in the position and orientation of the LED lens assembly, in the position of the electrode, and in the expression of Chr2 in SGNs. In each animal, oABR amplitude (approximated as the N1 amplitude) increased with light intensity (Figure, 6, B and C) and pulse duration (up to about 2 ms at 4 mW/mm<sup>2</sup>) (Figure 6D), and we observed little amplitude and shape variability between the individual oABR traces during repeated stimulations (Supplemental Figure 10). By visual inspection, we determined the light threshold to be the radiant exposure that caused a clear deviation of the mean difference potential from the baseline before stimulation. On average, we observed threshold responses at  $2.2 \pm 0.4$   $\mu$ J/mm<sup>2</sup> (for 2- to 5-ms stimuli), which is roughly 7–70 times lower (depending on the infrared laser pulse duration) than the threshold radiant exposure reported for infrared stimulation of the SGN compound action potential (48).

Response latency decreased with light intensity and reached, on average,  $3.14 \pm 0.26$  ms for the strongest stimuli tested (Figure 6E). This exceeds the latencies found with acoustic (typically 1.3 ms for 80 dB click-evoked aABRs) (Figure 1E and ref. 49) and electrical (approximately 0.3 ms) (34) stimulation. We assume

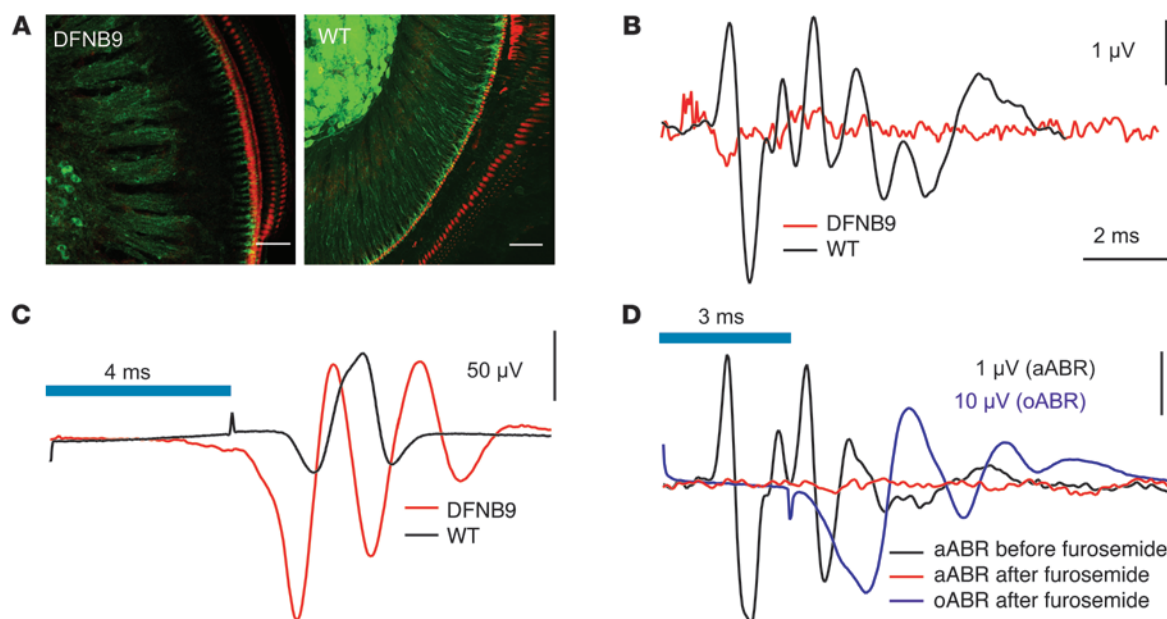


### Figure 7

Cochlear optogenetics restores auditory activity in deaf mice. **(A)** Maximum projection of confocal sections of apical cochlear coils from ChR2-positive otoferlin mutant (DFNB9 mouse model) and wild-type control mice following immunolabeling for GFP (green, labeling ChR2-YFP-expressing radial fibers and SGN somata) and actin (red, phalloidin-AF-568, labeling ChR-YFP-negative hair cells). Scale bars: 50  $\mu$ m. **(B)** Lack of aABRs in a representative ChR2-positive DFNB9 mouse (red, 120 dB clicks at 20 Hz, average of 5,800 trials; initial potential likely reflects cochlear microphonics or summing potentials of hair cells; ref. 51) and a wild-type control mouse (black, 80 dB clicks at 20 Hz, average of 800 trials). **(C)** oABRs could be elicited in the DFNB9 mouse after cochleostomy ( $\mu$ LED, 4 ms, 1 Hz, 1,000 trials). **(D)** Abolition of aABRs but preserved oABRs 30 minutes after s.c. furosemide injection.

that the oABR latency reflects the time required for ChR2 to depolarize the neuronal membrane potential to the action potential threshold (Figure 9 and ref. 31), which is governed by the number and conductance of active ChR2 channels. oABR amplitudes declined when stimulus rates were raised above 20 Hz (Figure 6F), but remained sizable (tens of  $\mu$ V) up to 70 Hz. ABR amplitudes decreased and latency increased during higher-frequency stimulation. In summary, ChR2-mediated transcochlear optogenetics induced oABRs with a 2- $\mu$ J threshold and a 3.1-ms minimal latency and were observed for stimulation rates up to 70 Hz.

**Restoring auditory afferent activity in mouse models of deafness.** Next, we tested the ability of cochlear optogenetics to activate the auditory pathway in mouse models of human deafness. As a model of early-onset genetic deafness, we chose a mouse line that carries the D1767G point mutation (NP\_001093865, NCBI) (50) in *Otof* (coding for the otoferlin mouse model of human deafness DFNB9). These *Otof*<sup>Pga/Pga</sup> mice have a severely defective transmitter release from IHCs (51). While their SGNs can generate a few action potentials in response to high-intensity sound stimulation (51), aABRs are absent (Figure 7B,  $n = 9$ , and refs. 50, 51). Here, we crossed the *Thy1.2*-driven *ChR2* transgene with *Otof*<sup>Pga/Pga</sup> mice to express ChR2 in their SGNs (Figure 7A). Transcochlear  $\mu$ LED stimulation elicited oABRs in these *Otof*<sup>Pga/Pga</sup>-*ChR2* mice ( $n = 9$ ) (Figure 7C), corroborating the hypothesis that deafness in *Otof*<sup>Pga/Pga</sup> mice is primarily caused by the presynaptic defect of their IHCs (51), while their SGNs are functional.

We also examined a model of acquired deafness by s.c. injection of 400  $\mu$ g/g furosemide into ChR2 mice to collapse their endocochlear potential (52), thereby abolishing mechanoelectrical transduction and afferent auditory signaling. We reasoned that

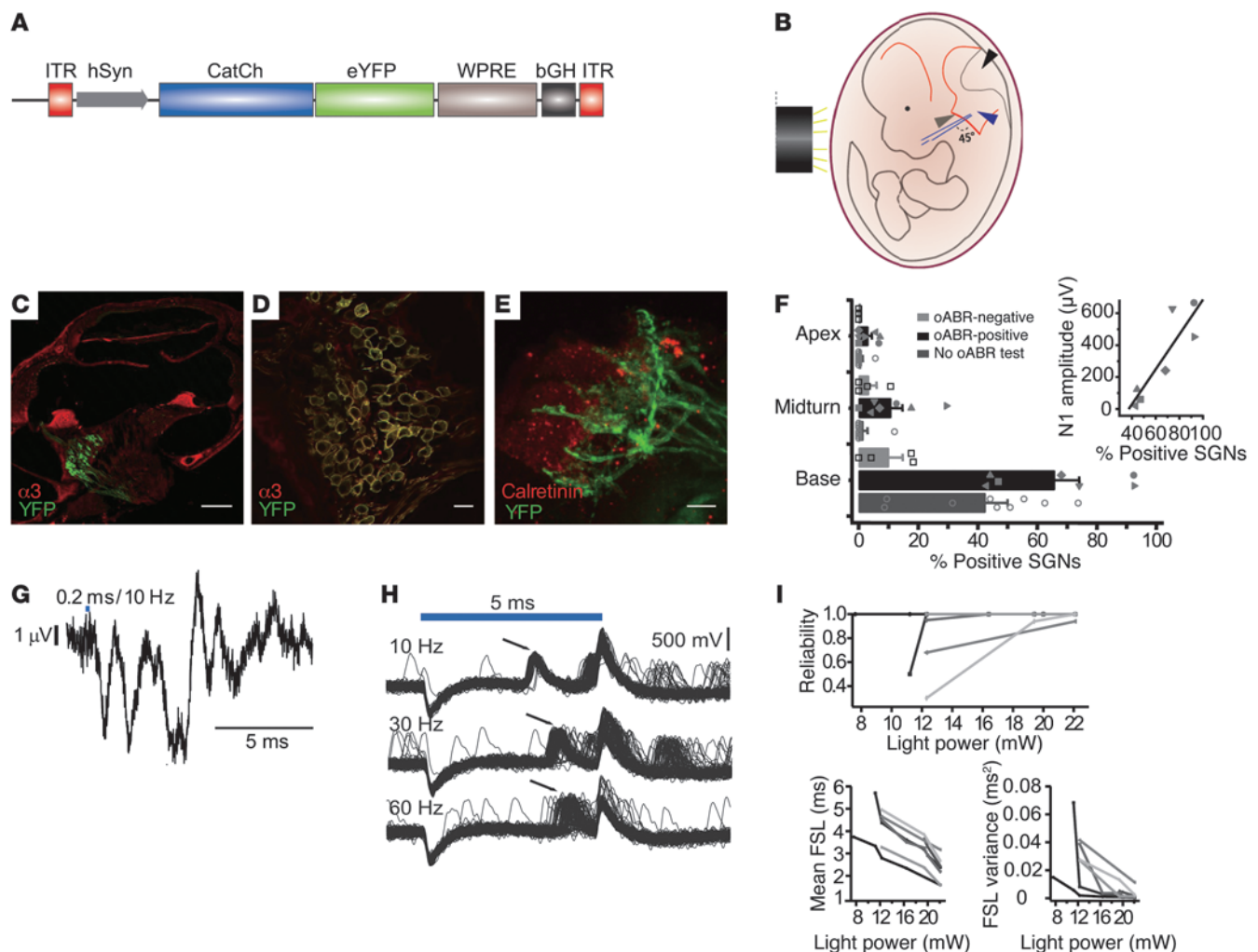
the oABRs should remain unaffected, because they solely build on optogenetic stimulation of SGNs independently of hair cell function. Indeed, the aABRs disappeared within 30 minutes, but transcochlear  $\mu$ LED stimulation readily elicited oABRs ( $n = 5$ ) (Figure 7D). In conclusion, these two examples demonstrate that optogenetic cochlear stimulation can activate the auditory pathway in mouse models of human deafness.

**AAV2/6-mediated expression of CatCh in mouse SGNs.** If cochlear optogenetics is to be used in other species and translated into clinical applications, a number of objectives must be addressed. Importantly, biologically safe and reliable protocols for genetic manipulation of SGNs are required. Thus far, viral and nonviral approaches have been reported (53–59). Here, we focused on using AAVs, which are good candidates, because they were successfully used to transduce murine SGNs (53, 54, 60) and do not compromise hearing (60–62). We used transuterine virus injections into the left otocyst of 8 to 14 available embryos 11.5 dpc (refs. 62, 63, and Figure 8, A and B). This met the requirements for screening 10 different viruses for their potential to transduce SGNs and was based on morphological and functional analysis of a sufficient number of treated animals (Supplemental Table 1). Efficient and selective transduction of SGNs was observed only for AAV2/6, which carried the transgene under the control of the human synapsin promoter (Figure 8A). Among the ChR2 variants with improved properties, we selected CatCh, which shows higher  $\text{Ca}^{2+}$  permeability and was reported to induce 70-fold greater neuron light sensitivity compared with that found in wild-type ChR2 (33). Immunohistochemistry of cochlear cryosections showed expression of CatCh-fused yellow





## technical advance

**Figure 8**

AAV2/6-mediated expression of CatCh renders murine SGNs light sensitive. **(A)** Viral construct scheme. **(B)** Illustration of injection site on an embryo. Black, gray, and blue arrowheads indicate the fourth ventricle, primary head vein, and location of otocyst, respectively. **(C)** Cochlear section of a P7, AAV2/6-HSYN-CatCh-YFP-injected mouse; immunolabeling for Na/K-ATPase  $\alpha 3$  subunit (red) and YFP (green) shows expression of CatCh in SGNs of the basal turn. Scale bar: 200  $\mu$ m. **(D)** Magnification of **C** showing CatCh expression in SGN membranes. Scale bar: 20  $\mu$ m. **(E)** Organ of Corti immunostaining shows extension of CatCh expression (YFP in green) in SGNs to the point where their neurites contact IHCs (calretinin in red). Scale bar: 20  $\mu$ m. **(F)** Transduction of SGNs along the cochlear turns in positive animals (38% of injected animals were negative and are not shown). Markers for animals are maintained in the inset: oABR N1 amplitude correlates with transduction efficiency. **(G)** oABRs in response to 200- $\mu$ s laser stimulation via an optical fiber inserted into the round window. **(H)** Precise and reliable spiking in a putative SGN in a CatCh-transfected mouse at stimulation rates up to at least 60 Hz (5-ms light pulses). **(I)** Quantification of first spiking response (indicated by arrows in **H**). Reliability of spiking (proportion of trials eliciting a spike during the stimulation time window) (top), mean first spike latencies (FSLs) (bottom left), and FSL variance (bottom right) in response to 5- to 10-ms flashes at different intensities. Grayscale values indicate seven different light-responsive neurons in the region of the AN and cochlear nucleus.

fluorescent protein (YFP) and Na<sup>+</sup>/K<sup>+</sup>-ATPase in SGNs (Figure 8, C and D). We found that CatCh was expressed in the membranes of SGN somata and in their neurites to the point of contacting calretinin-positive IHCs (Figure 8E). Expression persisted at least until postnatal day 59, with no obvious decay of expression levels (data not shown). The fraction of CatCh-YFP-positive SGN somata in Rosenthal's canal was highest in the cochlear base (Figure 8, C and F).

For functional analysis, we used laser stimulation of the basal cochlea via a 250- $\mu$ m plastic optical fiber inserted through the round window. oABRs could be elicited in ears with at least 40%

of the basal SGNs expressing CatCh-YFP (Figure 8F). In 2 of 8 ears with oABRs, we observed a response to stimuli as short as 200  $\mu$ s (Figure 8G). The oABRs varied substantially between the various ears tested, which was partly related to the transduction rate (Figure 8F), but probably also reflected stimulation efficiency, i.e., the projection of the light beam. We then performed extracellular recordings from single putative SGNs as described above (Figure 3A). We detected optogenetically evoked action potentials (Figure 8I), which, for strong stimuli (22.1 mW), occurred with shorter latencies ( $2.8 \pm 0.2$  ms,  $n = 9$  units in 2 mice,  $P < 0.001$ ) than those of putative SGNs in Chr2 mice

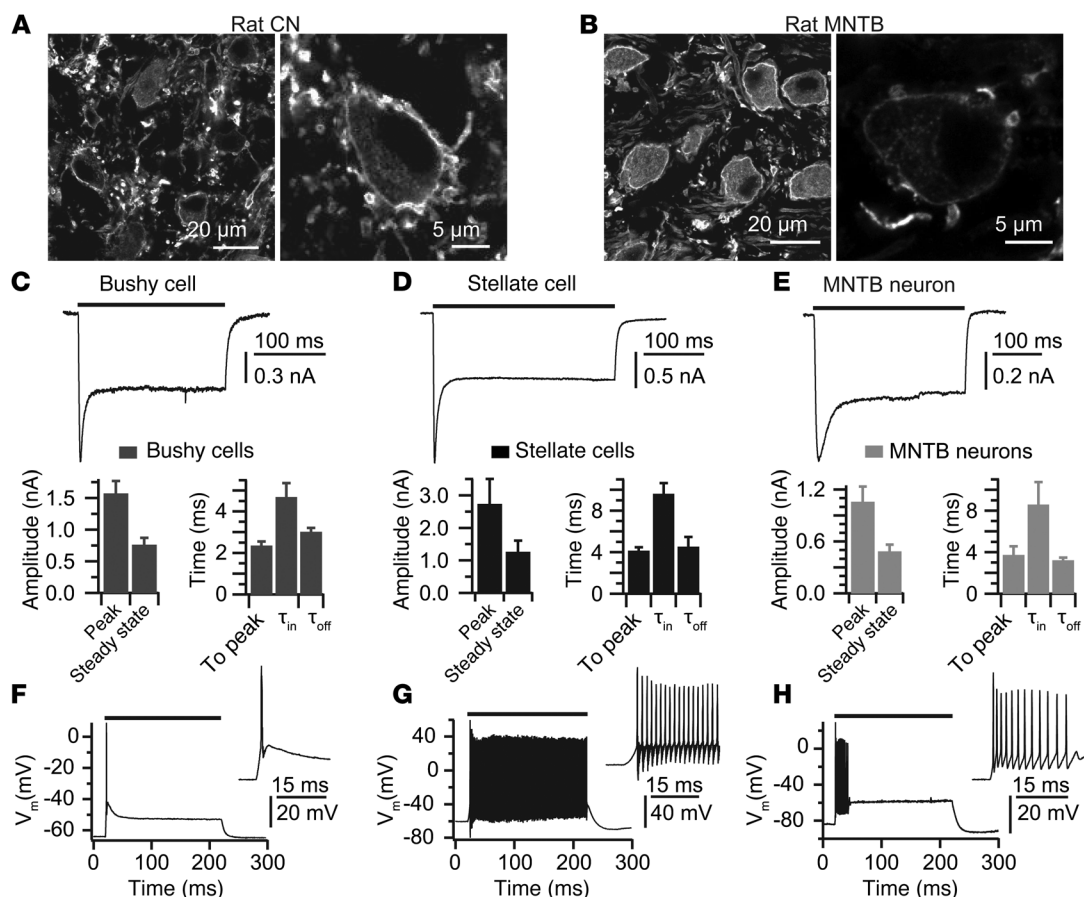


**Figure 9**

Photoreponses of auditory brainstem neurons in vitro. (**A** and **B**) Fluorescent images of principal cells stained for GFP to localize ChR2 expression in the cochlear nucleus and MNTB, respectively. Sample traces of phototransduction currents recorded from a bushy cell (**C**), a stellate cell (**D**), and an MNTB neuron (**E**) in response to laser light illumination over the time indicated by the line on top of the trace. Bar plots show the peak amplitude, steady-state amplitude, time to peak from light onset, and the inactivation and deactivation ( $\tau_{off}$ ) time constant obtained from single exponential fits (7 bushy, 4 stellate, and 6 MNTB cells). (**F–H**) Laser light stimulation elicited phasic firing in bushy cells, tonic firing in stellate cells, and adaptive firing in MNTB neurons.

(Figure 3A). The trial-to-trial variance of the first spike amounted to only  $0.02 \pm 0.01 \text{ ms}^2$ . The evoked spikes were more reliable and precise with shorter latency when the light power was increased (Figure 8I). Firing of SGNs in CatCh-AAV-injected animals required less laser power than in ChR2 transgenic mice (data not shown). While these differences in latency, spiking precision, and threshold are consistent with the described improved properties of CatCh (33), we cannot exclude that they are also related to different expression levels of CatCh versus ChR2 in SGNs. Next, we probed the spiking of single putative CatCh SGNs in response to 5-ms laser pulses presented at different rates and found that responses followed stimulation rates up to 60 Hz (Figure 8H), the current setup limit. To test whether the recorded neurons represented SGNs, additional acoustic stimulations were applied to four units. We could also drive spiking by acoustic stimulation in three of four neurons. The peristimulus time histograms (see Supplemental Figure 7 for an example) and the first spike latency (data not shown) of these neurons were compatible with those of SGNs (64). In summary, these data demonstrate that AAV2/6-mediated cochlear optogenetics is feasible.

**Direct optogenetic stimulation of auditory brainstem neurons.** Direct optogenetic stimulation of auditory brainstem neurons is of interest, from both a basic research and a translational point of view. It promises temporally precise and selective stimulation of single neurons or particular populations of neurons, which provide input into subsequent stages of auditory processing. Moreover, optogenetic stimulation may improve the performance of auditory brainstem implants, which are in clinical use for rehabilitation of hearing when a CI is not available due to a lack of functional SGNs, but which often fail to enable open speech understanding (7). Here, we turned to transgenic rats expressing ChR2-Venus under the control of the *Thy1.2* promoter (29). Immunolabeling studies showed ChR2 expression in SGNs (Supplemental Figure 6), in fibers and principal cells of the cochlear nucleus (Figure 9A), and in the medial nucleus of the trapezoid body (MNTB) (Figure 9B) of 3- to 4-week-old transgenic rats. Then, we used the whole-cell patch-clamp technique to study photoreponses in acute auditory brainstem slices upon blue light laser stimulation projected onto the preparation via an optical fiber. We used high-output light intensity ( $\sim 30 \text{ mW}$ ), aiming for saturation of current amplitudes



## technical advance

upon direct illumination of the target cell. Stellate and bushy cells of the anteroventral cochlear nucleus, identified by cell shape and firing pattern (tonic for stellate, phasic for bushy cells), and principal cells of the MNTB showed nanoampere photocurrents that reached a peak within 2 to 4 ms after light onset (Figure 9, C–E). Consistent with previous reports (e.g., ref. 31), we observed that Chr2-mediated photocurrents were partially inactivated (to ~47% of the peak amplitude) following an exponential time course, with time constants of 5 to 10 ms depending on the cell type (Figure 9, C–E). After light offset, deactivation occurred with millisecond kinetics (Figure 9, C–E).

In current-clamp recordings, photoresponses of stellate and bushy cells (Figure 9, F and G) mimicked the respectively tonic and phasic firing patterns found with electrical current injection (65), while MNTB principal cells showed adaptive firing (Figure 9H). On average, the peak of action potentials was reached  $2.1 \pm 0.1$  ms from light onset (data not shown). We occasionally encountered large transient currents riding on top of the postsynaptic photocurrent that were sensitive to CNQX, likely representing excitatory postsynaptic currents elicited by presynaptic photostimulation. Similar findings were obtained in a limited set of experiments in transgenic mice (data not shown).

## Discussion

Here, we provide a first proof of concept for optogenetic stimulation of the cochlea in rodents. We characterized the light-induced activation of the ascending auditory pathway in Chr2 transgenic mice and rats, the restoration of auditory system responses in mouse models of human deafness, and the feasibility of virus-mediated optogenetics in mouse SGNs. We found what we believe to be the first evidence for improved frequency resolution with optogenetic stimulation compared with that achieved with monopolar electrical stimulation. We explored various optical stimulation strategies and characterized the morphological constraints by phase-contrast x-ray tomography in mouse and rat. Finally, we characterized the photoresponses of auditory brainstem neurons by patch-clamp recordings. Our study lays the groundwork for advancing optogenetics as a tool for auditory research and future clinical applications.

*Optogenetic stimulation of auditory neurons.* Why consider optical stimulation for auditory research and prosthetics? Generating tailored activity in small SGN populations in the absence of micromechanical spectral mixing in the cochlea offers unprecedented opportunities for auditory research. Optical stimulation has the potential to improve auditory prosthetics, because a larger number of independent stimulation channels would enable innovative strategies for coding frequency and intensity in order to enhance the perception of speech, prosody, and music.

Here, we studied optogenetic stimulation of auditory neurons in Chr2 transgenic mice and rats (refs. 29, 32, and Figures 1–7 and 9) as well as in mice expressing the Chr2 variant CatCh (33) in their SGNs following embryonic viral gene transfer (Figure 8). The *Thy1.2* promoter drove neuronal Chr2 expression in transgenic mice and rats throughout the spiral ganglion, cochlear nucleus, and MNTB, while hair cells and supporting cells within the organ of Corti were negative. Immunohistochemistry suggested broad membrane expression of Chr2, which supported robust optogenetic spike generation in auditory neurons and did not noticeably alter auditory function. The patch-clamp demonstrated large photocurrents in auditory brainstem neurons, and we assume that

SGNs behave similarly. These recordings demonstrate that Chr2 transgenic rats (and mice) can be used for optical stimulation of auditory brainstem circuitry and are consistent with another recent report (66).

AAV2/6, carrying the transgene under the human synapsin promoter, was identified from among ten viral vectors (including various AAV serotype-promoter combinations, herpes simplex, and hemagglutinating virus of Japan envelope vector) to drive the most efficient and stable (in animals up to at least 8 weeks of age) opsin expression. Transfection and expression were specific to SGNs, where, again, the opsin was targeted to the membranes of neurites and somata. In contrast to the homogenous transgenic Chr2 expression, a strong basoapical gradient was found for virus-mediated Chr2 expression in the spiral ganglion. We hope to overcome this in future work by increasing the virus titer. In addition, protocols for efficient and safe postnatal AAV-mediated gene transfer into SGNs need to be established in rodents and later in nonhuman primates.

Using rodent models, we developed transcochlear and intracochlear optogenetic stimulation strategies using the blue light of LEDs or fiber-coupled lasers. Previous optical cochlea stimulation was restricted to laser light, while in our study,  $\mu$ LEDs were used successfully for both transcochlear and intracochlear stimulation. We found phase-contrast x-ray tomography to be useful for measuring the dimensions of mouse and rat cochlear ducts (Supplemental Figure 8), the position of the cochleostomy relative to the tonotopic map (Figure 4), and the intracochlear placement and orientation of emitters (data not shown).

*Properties of optogenetic stimulation of the auditory pathway.* Optogenetics permits optical SGN stimulation with low energy requirements. We could elicit oABRs with 2  $\mu$ J of light entering the approximately 1 mm<sup>2</sup> cochleostomy, which is lower than that reported for infrared stimulation (intracochlear SGN compound action potentials: 16–150  $\mu$ J/mm<sup>2</sup>; ref. 48), but still higher than the energy per pulse used in electrical CIs (approximately 0.2  $\mu$ J; ref. 19). We anticipate that the required energy per pulse can be further reduced by using intracochlear emitters in close apposition to the spiral ganglion (as simulated in Supplemental Figure 9) and by increased SGN light sensitivity via enhanced expression of optimized channelrhodopsin variants. This will be important in order to enable acceptable battery lifetimes when using optogenetics in future clinical CIs. While these CIs will likely use 10-fold lower pulse rates per channel than electrical implants (hundreds versus a few thousand Hz), they will have a greater number of channels than current CIs (hundred[s] versus dozens).

The latencies of single SGN and SGN population responses were longer for optical than for acoustic stimulation, probably owing to the time required for the SGNs to reach the action potential threshold after Chr2 activation (Figure 8 and ref. 32). SGN latencies decreased with increasing light intensity (Figures 6 and 8), likely via increasing the light-activated depolarizing conductance. This may further be achieved by enhanced abundance, light sensitivity, or conductance of the channelrhodopsin. In this context, it is interesting to note that we found first spike latencies of single SGNs similar to those observed with acoustic clicks when using viral expression of the optimized Chr2 variant CatCh and strong light stimulation. Since oABRs and single SGN responses of CatCh-injected mice were generally comparable to those of transgenic Chr2 mice, in which cochlear optogenetics could, potentially, also stimulate the olivocochlear efferent system, this, if occurring at all, seemed to





have little impact. The temporal precision of spike generation with optogenetics (trial-to-trial variance of  $0.020 \text{ ms}^2$  for CatCh SGNs) was intermediate between acoustic (clicks:  $0.700 \text{ ms}^2$ ) and electrical ( $0.004 \text{ ms}^2$ ) (67) stimulation. The amplitude of oABRs declined with increasing stimulation rates above 20 Hz. Our present data indicate that CatCh-expressing SGNs can follow at least 60 Hz of optogenetic stimulation. Future recordings of single auditory nerve fibers will need to establish the maximum rate at which SGNs can follow optogenetic stimulation. Expression in SGNs of ChR2 variants with faster deactivation (68) will likely enhance high temporal bandwidth auditory signaling in cochlear optogenetics.

High-frequency resolution of optical stimulation due to spatial confinement is one of the most attractive prospects of cochlear optogenetics. In this proof-of-principle study, we used three approaches for a first assessment of cochlear spread of excitation. Using transcochlear stimulation, we found masking of aABRs over a frequency range of less than an octave by  $\mu$ LED located hundreds of micrometers away from the stimulated SGNs. We found that illumination by an optical fiber in the scala tympani elicited activation of the basal portion of the spiral ganglion. Furthermore, when analyzing the current source density in the IC, we found that the spread of cochlear excitation was comparable to that achieved with acoustic stimulation and narrower than with electrical stimulation. We note that we used LFPs in response to suprathreshold stimuli for all modalities. As a population measure, the spread of the current sink identified by CSD analysis can be interpreted as revealing the population of neurons — with varying characteristic frequencies — that are activated by the various stimulation modalities (41, 43). The tuning of individual neurons within this activated population cannot be assessed using our technique and might differ between stimulus regimes. Therefore, these results can only serve as a first and relative assessment, as they likely provide an upper estimate for the spread of cochlear excitation. Future studies using intracochlear multichannel optical stimulation of the spiral ganglion should assess the spread of excitation based on an analysis of IC activity at various light intensities and compare this with acoustic and electrical stimulation at various intensities. As a first step, we modeled blue  $\mu$ LED illumination using realistic dimensions of the mouse cochlea and predicted a spread of excitation of one-third of an octave, even without focusing.

**Outlook.** Future work aimed at advancing optogenetics for use in auditory research and for clinical translation should include: (a) the development of reliable multichannel optical stimulation technology; (b) studies of biosafety for optical stimulation; (c) the optimization of channelrhodopsins as well as of virus-mediated gene transfer for the efficient and safe long-term expression of channelrhodopsin DNA in auditory neurons; and (d) the comprehensive characterization and further improvement of coding by optogenetic stimulation in comparison with electrical and physiological coding. Future optic or hybrid (optic-electrical) CIs will likely contain hundred(s) of light-emitting elements such as LEDs, vertical cavity surface-emitting lasers, or waveguides with apertures of tens of micrometers. We argue that well-positioned intracochlear emitters will likely reduce the variability of optogenetic responses between animals that was prominent in the present study. While the potential phototoxicity of cochlear optogenetics remains to be assessed in future studies, we note that relevant work on other neurons suggests that it is not a major safety concern (69, 70). Rapid progress is being made in the identification, site-directed mutagenesis, and characterization of optogenetic tools (reviewed in ref. 25).

Opsins tailored to cochlear optogenetics will ideally combine high light sensitivity and rapid deactivation kinetics for energy efficiency and high rate stimulation as well as red-shifted action spectra for minimizing scattering and potential phototoxicity in the spiral ganglion. At present, AAVs appear to be the approach of choice for cochlear optogenetics. AAVs have been shown to be efficient in gene replacement therapy in the mouse inner ear (71) and to leave intact cochlear function (61, 62, 71). Injections of AAVs into the cochlear nucleus, including the subsequent expression and activation of ChR2 and halorhodopsin, did not lead to detrimental effects on hearing for at least 18 months in rats (66). Moreover, AAVs have been successfully used in experimental and clinical retinal gene replacement (72). However, while it is promising that single injections of AAVs carrying the DNA of RPE65 into the eye have restored lifelong visual function in mice and dogs and 5-year function so far in clinical trials (for the eye, ref. 73, and for systemic gene therapy applications, ref. 74), careful evaluation of immune responses is required for cochlear applications.

Finally, a comprehensive morphological, physiological, and behavioral analysis of cochlear optogenetics in rodents and later in nonhuman primates is required to characterize the temporal, frequency, and intensity resolution of signal coding. We expect these efforts to pave the way for innovative auditory research and optical restoration of hearing.

## Methods

### Animals

Experiments were performed on 4- to 20-week-old transgenic *ChR2* mice (32), otoferlin mouse mutants (50) carrying the *ChR2* transgene, and C57BL/6 wild-type mice. Moreover, transgenic rats expressing ChR2 under the murine *Thy1.2* promoter on a Wistar background were used (29). Here, ChR2 was coupled to Venus, a YFP variant.

### Transuterine injections of AAVs

For in vivo transduction, anesthesia was induced with a mixture of ketamine and xylazine ( $0.125/5 \text{ mg/kg}$ ) and maintained with isoflurane ( $1\%-2\%$ ). Viral inoculum ( $\sim 250 \text{ nl}$ ,  $4 \times 10^8$  particles/ $\mu\text{l}$ ) was microinjected through the uterus into the mouse ootocyst from E11.5 to E12.5 as previously described (62, 63). Only the left ootocyst of each embryo was injected. The uninjected contralateral ear served as an internal control.

### Immunostaining and confocal microscopy

Immunostaining was performed essentially as described (51, 62, 75). Sections of the cochlea used for Figure 1A were cut after EDTA decalcification. Phalloidin-AF-568, rabbit anti-GFP (both 1:200; Invitrogen), mouse anti-neurofilament (NF 200, 1:400; Sigma-Aldrich), and appropriate secondary antibodies (1:200; Invitrogen) were used. For Figures 1 and 7, the cochleae were decalcified for 10 minutes in Morse's solution and sectioned, and Na/K-ATPase  $\alpha 3$  subunit (1:300; Invitrogen) and Alexa Fluor 488-conjugated anti-GFP (1:500; Invitrogen) antibodies were used for staining. The images were acquired using a Leica TCS SP2 laser scanning confocal microscope.

### Animal surgery

Mice were anesthetized with i.p. administration of a mixture of urethane ( $1.32 \text{ mg/kg}$ ), xylazine ( $5 \text{ mg/kg}$ ), and buprenorphine ( $0.1 \text{ mg/kg}$ , for single-unit and IC recordings), or of ketamine ( $0.125 \text{ mg/kg}$ ) and xylazine ( $5 \text{ mg/kg}$ , for ABR recordings). The animals were then placed onto a custom-designed heat plate (for maintaining body temperature at  $37^\circ\text{C}$ ) on a vibration isolation table in a sound-proof chamber (IAC GmbH).



## technical advance

**Cochleostomy.** The left bulla was reached using a retroauricular approach and opened to expose the cochlea. Gentle shaving of the bony cochlear capsule was performed to open a small (500–800  $\mu\text{m}$ ) cochleostomy, leaving intact the membranous labyrinth. In order to avoid contralateral acoustic stimulation of ABRs in light-on-tone masking experiments, the contralateral cartilaginous outer ear was cut, the tympanic membrane and ossicular chain were removed, and the cochlea was mechanically destroyed.

**SGN and cochlear nucleus recordings.** For auditory nerve recordings, a tracheostomy was performed before the animals were positioned in a custom-designed stereotaxic head holder. The left occipital bone and cerebellum were partially removed to expose the surface of the cochlear nucleus.

**IC recordings.** For recordings from the IC, the skin covering the forehead was cut and reflected laterally. A metal screw was glued onto the exposed skull using dental cement and fixed onto the bar of a custom-made stereotaxic device. We used craniometric references to either perform a small craniotomy or a trepanation over the right IC before the dura was carefully removed.

### Optical stimulation

We used four approaches for optical stimulation of the cochlea: (a) As shown in Figures 1, 2, and 6, for the most reliable quantification of irradiance, we used a blue power LED (Avago Technologies) coupled to a plano-convex lens ( $f = 100$  mm, arc: 350–650 nm; Thorlabs GmbH) mounted onto a micromanipulator and focused on a cochleostomy. Irradiance was measured during 20-s stimulation using a thermal power sensor (0.19–25  $\mu\text{m}$ , 2 W; Thorlabs GmbH) placed behind a light-blocking plate with a 1-mm<sup>2</sup> pinhole in the focal plane of the lens. (b) For the experiments shown in Figures 3, 5, 8, and 9, we used a 250- $\mu\text{m}$  optical fiber coupled to a 473-nm laser (MBL473, 50 mW DPSS; Changchun). Irradiance was calibrated with a laser power meter (LaserCheck; Coherent Inc.). For the experiment shown in Figure 3, the fiber was located on a small cochleostomy, and for the experiments depicted in Figures 5 and 8, the optical fiber was inserted into the round window and fixed in place with cyanoacrylate and/or dental cement. (c) For the experiments shown in Figures 4 and 7, we used blue LEDs with a 200  $\mu\text{m} \times 200$   $\mu\text{m}$  active surface ( $\mu\text{LED}$ ; Cree). We removed the plastic case, trimmed the support, soldered the  $\mu\text{LED}$  to wires, and encapsulated the assembly using epoxy. For mechanical stability and electrical insulation, a section of the wires was funneled through a thin glass pipette and mounted on a manipulator (Narishige International Ltd.). Irradiance was approximated by placing the assembly into the aperture of a LaserCheck hand-held power meter. (d) For the experiment shown in Supplemental Figure 1, we used an intracochlear  $\mu\text{LED}$  implant, in which the  $\mu\text{LED}$  was bonded and embedded in silicone along with 10- $\mu\text{m}$  wires.

### ABR recordings

ABRs were recorded by scalp needle electrodes underneath the pinna, on the vertex, and on the back near the legs. For stimulus generation and presentation, data acquisition, and off-line analysis, we used a TDT III System (Tucker-Davis Technologies) and custom-written MATLAB software (The MathWorks, Inc.). Sound pressure levels are provided in dB sound pressure level (SPL) root mean square (RMS) (tonal stimuli) or dB SPL peak equivalent (PE) (clicks) and were calibrated with a 0.25-inch Brüel and Kjaer microphone (D 4039; Brüel & Kjaer GmbH). Tone bursts (10 ms plateau, 1 ms cos<sup>2</sup> rise/fall) or clicks (0.03 ms) were ipsilaterally presented at 20 Hz in a free field using a JBL 2402 speaker (JBL GmbH & Co.). The difference potential between vertex and mastoid subdermal needles was amplified using a custom-designed amplifier, sampled at a rate of 50 kHz for 20 ms, and filtered off-line (300–3,000 Hz for aABRs and 1–10,000 Hz for eABRs

and oABRs). The hearing threshold was determined by visual inspection as the lowest stimulus intensity that evoked a reproducible response waveform in the recorded traces.

### Extracellular single-unit recordings

For auditory nerve recordings, a glass microelectrode (25 MOhm) was advanced through the posterior end of the anteroventral cochlear nucleus, aiming toward the internal auditory canal using an Inchworm micropositioner (EXFO Burleigh). Extracellular action potentials were amplified using an ELC-03XS amplifier (NPI Electronic), filtered (band pass, 300–3000 Hz), and digitized (TDT System 3) using custom-written MATLAB software. Data were further analyzed and prepared for display off-line using custom-written MATLAB software.

### LFP recordings in the IC

Optical stimulation was performed with round window insertion [see (b) under “Optical stimulation” in Methods]. We used 6-ms laser pulses at a stimulation rate of 6 Hz. Responses to 100 stimulus repetitions were averaged. Acoustic stimuli consisted of pure tones of 31 kHz at 80 dB SPL (RMS), which were generated by custom-written MATLAB routines and presented at a stimulation rate of 2 Hz in random order. Responses to 5 stimulus repetitions were averaged. Stimuli were converted into analog waveforms by a sound card (OCTA-CAPTURE; Roland) and presented via an ultrasonic speaker (Vifa; Avisoft Bioacoustics). A rodent electrical CI (MED-EL) was used for electrical stimulation and inserted into the cochlea via the round window. Biphasic current pulses (80  $\mu\text{s}$  phase duration, 20  $\mu\text{s}$  interphase duration, 500  $\mu\text{A}$ , 6 Hz stimulation rate) were used to stimulate neurons in the vicinity of the stimulation electrode. Responses to 100 stimulus repetitions were averaged. To drive either a DPSS laser (473 nm; CNI Laser) for optical stimulation or a constant current source (A365; WPI Inc.) for electrical stimulation, custom-built electronics converted sound bursts from the sound card into TTL pulses of the same duration.

After a posterior craniotomy overlying the IC (approximately  $-5.2$  mm in the anterior-posterior direction from the bregma and 1.25 mm in the mediolateral direction from the midline) and removal of the dura, a single-shank, 16-channel neuronexus probe (100- $\mu\text{m}$  channel spacing; NeuroNexus) was inserted into the ICC to record (sampling rate, 32 kHz) depth profiles of LFPs (Digital Lynx SX; Neuralynx). In the experiments, the multichannel probe was initially inserted such that the topmost channel was visible at the surface of the IC. Then, responses to either acoustic, optical, or electrical stimulation were recorded. In order to fully sample the ICC, after recording in this position the electrode was further advanced until the bottom-most channel was located at a depth of approximately 2 mm. Depth profiles of LFPs were transformed into CSD patterns as described earlier (44). The CSD analysis identifies excitatory inputs onto a population of neurons as current sinks and passive return currents as sources (Figure 5). Sinks that exceeded three standard deviations from baseline (30-ms window prior to stimulus onset) for at least 5 ms and had a spatial extent of at least 200  $\mu\text{m}$  were considered significant. The strongest sink within the first 30 ms after stimulus was identified as a proxy for excitatory drive to the IC. For identified sinks, the centroid and the peak were calculated. Tone bursts of various frequencies from 2 to 64 kHz were used to calibrate the tonotopic location of the recording probe (Supplemental Figures 3 and 4). The centroid depth increased with an increasing stimulation frequency (4 kHz centroid:  $\sim 0.4$  mm depth; 32 kHz centroid:  $\sim 1.2$  mm depth). The slope of change of the centroid depths with changing stimulation frequency as well as the absolute depth of the centroid locations were quantitatively similar to published single-unit data (45, 76, 77).



### *In vitro electrophysiology*

Coronal slices (220  $\mu\text{m}$ ) of rat auditory brainstem were prepared as follows: Brains were carefully dissected and immediately immersed in ice-cold low sodium, low calcium cutting solution containing (in mM): 75 NaCl, 26  $\text{NaHCO}_3$ , 75 sucrose, 1.25  $\text{NaH}_2\text{PO}_4$ , 2.5 KCl, 25 glucose, 7  $\text{MgCl}_2$ , and 0.25  $\text{CaCl}_2$ , aerated with 95%  $\text{O}_2$  and ~5%  $\text{CO}_2$  (carbogen). Meninges were removed from the ventral aspect of the brainstem. The pons-midbrain junction was cut to separate the forebrain from the brainstem and was then glued onto the stage of a Leica 1200 S vibrating microtome. Slices were incubated at 34°C for 30 minutes in artificial cerebrospinal fluid (aCSF) containing: 125 mM NaCl, 26 mM  $\text{NaHCO}_3$ , 20 mM glucose, 2.5 mM KCl, 1.25 mM  $\text{NaH}_2\text{PO}_4$ , 1 mM  $\text{MgCl}_2$ , 1.5 mM  $\text{CaCl}_2$ , 4 mM Na L-lactate, 2 mM Na pyruvate, and 0.4 mM Na L-ascorbate, aerated with carbogen and thereafter kept at room temperature until recording. Experiments were carried out under constant superfusion with prewarmed aCSF at flow rates of 3 to 4 ml/min. The temperature was monitored by a thermistor placed between the inflow site and the tissue slice and warmed to 34°C to 36°C by an in-line solution heater (SH-27B with TC-324B controller; Warner Instruments). Pipettes were pulled from borosilicate glass (outer diameter [OD] 1.5 mm, inner diameter [ID] 0.86 mm; Science Products) at a resistance of 1.5 to 3 M $\Omega$  when filled with the following solution for the voltage-clamp recordings: 35 mM CsF, 100 mM CsCl, 10 mM EGTA, 10 mM HEPES, and 1 mM QX-314 (Alamone Labs); or with the following for the current-clamp recordings: 110 mM K-gluconate, 10 mM NaCl, 10 mM HEPES, 4.5 mM  $\text{MgCl}_2$ , 8 mM EGTA, 4 mM MgATP, 0.3 mM NaGTP, 10 mM  $\text{Na}_2$ -phosphocreatine, with the pH adjusted to 7.3, 300 mOsm.

### *Light-on-tone masking experiments*

After positioning a blue  $\mu\text{LED}$  into contact with the cochleostomy, aABRs to tone bursts (probe: duration of 12 ms, 1 ms rise/fall) were recorded as described above using a stimulus rate of 5 Hz. Then, 40-ms light pulses (masker: 4 mW/mm<sup>2</sup>) were introduced to mask the sound response. The probe tones were delayed by 20 ms with respect to the light stimulus to enable separation of oABR and aABR waveforms. Sound thresholds were determined before starting the light stimulation as described above. Three hundred responses to the tone bursts were averaged for each condition and filtered between 300 and 3,000 Hz. A reduction of suprathreshold aABR amplitudes was investigated in a different set of experiments, in which tone bursts (12-ms) were preceded by a 3-ms light stimulus at 10-ms intervals. aABRs were evoked by tone bursts of different frequencies at 90 dB. Possible masking was analyzed by comparing the amplitude of aABR wave 1 in the absence and presence of  $\mu\text{LED}$  stimulation.

### *X-ray imaging*

Phase-contrast tomography at a compact laboratory x-ray source was used to identify the position of the cochleostomy relative to the cochlear tonotopic map (Figure 4 and Supplemental Video 1) and to estimate the available scalar space for an intracochlear implant (Supplemental Figure 8). The method is based on cone-beam in-line phase-contrast tomography (78) and a fast Fourier-based phase reconstruction procedure (79). The x-ray source (JXS R5 prototype; Excillum AB), equipped with a solid molybdenum target and operating at 60 kVp and 0.07 mA, was combined with a scintillator-based fiber-coupled CCD detector (6.5  $\mu\text{m}$  pixel size; Photonic Science). Spatial resolution and contrast of the x-ray imaging system revealed a thin and weakly absorbing basilar membrane inside a strongly absorbing bony cochlear capsule. Total accumulation time for a 3D dataset was about 6 hours. A detailed dis-

cussion on the properties of this imaging method and further imaging results are presented in ref. 35. Segmentation and 3D visualization of the reconstructed volume was performed with an Avizo Fire 7 (Visualization Sciences Group, FEI Company). Automatic histogram-based segmentation was used to visualize bony structures. The basilar membrane, Rosenthal's canal, scala tympani, scala vestibuli, and media, as well as the cochleostomy were traced with semiautomatic segmentation. To identify the tonotopic position of the cochleostomy relative to the cochlear tonotopic map, markers were set at different positions along the basilar membrane. A spline curve was fitted to the markers and was used to identify the position of the cochleostomy relative to the tonotopic map of the cochlea (Figure 4 and Supplemental Video 1). To estimate the available space for an intracochlear implant, the size of the scala tympani was measured as a function of the distance from the base (Supplemental Figure 8).

### *Statistics*

Data were checked for normality and equal variances and were consequently tested with parametric procedures or, in the case of violations of either normality or variance equality, with nonparametric procedures. Statistical differences between two groups were assessed with 2-tailed Student's *t* tests. Multiple groups were evaluated using Kruskal-Wallis ANOVA models, followed by post-hoc tests (Dunn's multiple comparison test) if appropriate. *P* values of less than 0.05 were considered significant. Data are presented as the means  $\pm$  SEM.

### *Study approval*

All experiments were conducted in accordance with NIH guidelines for the care and use of animals in research and with the ethical standards defined by the German law for the protection of experimental animals. Experiments were approved by the University of Göttingen board for animal welfare and the animal welfare office of the state of Lower Saxony.

### *Acknowledgments*

We thank Mercedes Muske for contributing to the immunohistochemical analysis; Hugo Cruces Solis for providing the histological image of the IC; Ursula Stalmann for supplying aABR data on aging mice; Mark A. Rutherford, Nobert Dillier, Werner Hemmert, and Fred Wolf for comments on the manuscript; and Christiane Senger-Freitag, Sandra Gerke, Peter Wenig, and Nina Dankenbrink-Werder for technical assistance. We would like to thank Karl Deisseroth and Oliver Schlüter for providing virus, John Brigande for introducing us to transuterine gene transfer, and Simone Kurt, Andrej Kral, John Middlebrooks, Holger Schulze, and Maike Vollmer for discussions and help with electrical stimulation and IC recordings. This work was supported by the German Federal Ministry of Education and Research (Bernstein Focus for Neurotechnology grant 01GQ0810, to T. Moser, and MED-EL Germany); the German Research Foundation through the Center for Nanoscale Microscopy and Molecular Physiology of the Brain (FZT 103, to S. Kügler, T. Salditt, and T. Moser and SFB889, to N. Strenze and T. Moser); by Competitive Research Program (CRP) funds from the National Research Foundation, Singapore; and the World Class Institute (WCI) Program of the National Research Foundation of Korea (NRF), funded by the Ministry of Education, Science and Technology of Korea (MEST) (NRF WCI 2009-003, to G. Augustine).

Received for publication February 13, 2013, and accepted in revised form November 21, 2013.





## technical advance

Address correspondence to: Tobias Moser, InnerEarLab, Department of Otolaryngology and Collaborative Research Center 889, University of Göttingen Medical Center, 37099 Göttingen, Germany. Phone: 49.551.39.8968; Fax: 49.551.39.12950; E-mail: [tmoser@gwdg.de](mailto:tmoser@gwdg.de).

Victor H. Hernandez's present address is: Department of Chemistry, Electronics and Biomedical Engineering, Division of Sciences and Engineering, University of Guanajuato, Guanajuato, Mexico.

1. Clark GM. The multiple-channel cochlear implant: the interface between sound and the central nervous system for hearing, speech, and language in deaf people—a personal perspective. *Philos Trans R Soc Lond B Biol Sci*. 2006;361(1469):791–810.
2. Moore DR, Shannon RV. Beyond cochlear implants: awakening the deafened brain. *Nat Neurosci*. 2009;12(6):686–691.
3. Wilson BS, Dorman MF. Cochlear implants: current designs and future possibilities. *J Rehabil Res Dev*. 2008;45(5):695–730.
4. Middlebrooks JC, Bierer JA, Snyder RL. Cochlear implants: the view from the brain. *Curr Opin Neurobiol*. 2005;15(4):488–493.
5. Zeng F-G, Rebscher S, Harrison WV, Sun X, Feng H. Cochlear implants: system design, integration, and evaluation. *IEEE Rev Biomed Eng*. 2008;1:115–142.
6. Rubinstein JT. Paediatric cochlear implantation: prosthetic hearing and language development. *Lancet*. 2002;360(9331):483–485.
7. Colletti V, Shannon RV, Carner M, Veronese S, Colletti L. Progress in restoration of hearing with the auditory brainstem implant. *Prog Brain Res*. 2009;175:333–345.
8. Kral A, Hartmann R, Mortazavi D, Klinke R. Spatial resolution of cochlear implants: the electrical field and excitation of auditory afferents. *Hear Res*. 1998;121(1–2):11–28.
9. Shannon RV. Multichannel electrical stimulation of the auditory nerve in man. II. Channel interaction. *Hear Res*. 1983;12(1):1–16.
10. Friesen LM, Shannon RV, Baskent D, Wang X. Speech recognition in noise as a function of the number of spectral channels: comparison of acoustic hearing and cochlear implants. *J Acoust Soc Am*. 2001;110(2):1150–1163.
11. Fishman KE, Shannon RV, Slattery WH. Speech recognition as a function of the number of electrodes used in the SPEAK cochlear implant speech processor. *J Speech Lang Hear Res*. 1997;40(5):1201–1215.
12. Donaldson GS, Kreft HA, Litvak L. Place-pitch discrimination of single- versus dual-electrode stimuli by cochlear implant users (L). *J Acoust Soc Am*. 2005;118(2):623–626.
13. Srinivasan AG, Shannon RV, Landsberger DM. Improving virtual channel discrimination in a multi-channel context. *Hear Res*. 2012;286(1–2):19–29.
14. Middlebrooks JC, Snyder RL. Auditory prosthesis with a penetrating nerve array. *J Assoc Res Otolaryngol*. 2007;8(2):258–279.
15. Zeng F-G, et al. Speech dynamic range and its effect on cochlear implant performance. *J Acoust Soc Am*. 2002;111(1 pt 1):377–386.
16. Izzo AD, et al. Selectivity of neural stimulation in the auditory system: a comparison of optic and electric stimuli. *J Biomed Opt*. 2007;12(2):021008.
17. Matic AI, Walsh JT Jr, Richter C-P. Spatial extent of cochlear infrared neural stimulation determined by tone-on-light masking. *J Biomed Opt*. 2011;16(11):118002.
18. Richter C-P, et al. Spread of cochlear excitation during stimulation with pulsed infrared radiation: inferior colliculus measurements. *J Neural Eng*. 2011;8(5):056006.
19. Zierhofer CM, Hochmair-Desoyer JJ, Hochmair ES. Electronic design of a cochlear implant for multichannel high-rate pulsatile stimulation strategies. *IEEE Trans Rehabil Eng*. 1995;3(1):112–116.
20. Nagel G, et al. Channelrhodopsin-2, a directly light-gated cation-selective membrane channel. *Proc Natl Acad Sci U S A*. 2003;100(24):13940.
21. Bamann C, Kirsch T, Nagel G, Bamberg E. Spectral characteristics of the photocycle of channelrhodopsin-2 and its implication for channel function. *J Mol Biol*. 2008;375(3):686–694.
22. Ritter E, Stehfest K, Berndt A, Hegemann P, Bartl FJ. Monitoring light-induced structural changes of Channelrhodopsin-2 by UV-visible and Fourier transform infrared spectroscopy. *J Biol Chem*. 2008;283(50):35033–35041.
23. Berndt A, Prigge M, Gradmann D, Hegemann P. Two open states with progressive proton selectivities in the branched channelrhodopsin-2 photocycle. *Biophys J*. 2010;98(5):753.
24. Kato HE, et al. Crystal structure of the channelrhodopsin light-gated cation channel. *Nature*. 2012;482(7385):369–374.
25. Yizhar O, Fenno LE, Davidson TJ, Mogri M, Deisseroth K. Optogenetics in neural systems. *Neuron*. 2011;71(1):9–34.
26. Hegemann P, Möglich A. Channelrhodopsin engineering and exploration of new optogenetic tools. *Nat Meth*. 2010;8(1):39–42.
27. Bi A, et al. Ectopic expression of a microbial-type rhodopsin restores visual responses in mice with photoreceptor degeneration. *Neuron*. 2006;50(1):23–33.
28. Lagali PS, et al. Light-activated channels targeted to ON bipolar cells restore visual function in retinal degeneration. *Nat Neurosci*. 2008;11(6):667–675.
29. Tomita H, et al. Visual properties of transgenic rats harboring the channelrhodopsin-2 gene regulated by the Thy-1.2 promoter. *PLoS ONE*. 2009;4(11):e7679.
30. Busskamp V, et al. Genetic reactivation of cone photoreceptors restores visual responses in retinitis pigmentosa. *Science*. 2010;329(5990):413.
31. Wang H, et al. High-speed mapping of synaptic connectivity using photostimulation in Channelrhodopsin-2 transgenic mice. *Proc Natl Acad Sci U S A*. 2007;104(19):8143.
32. Arenkiel BR, et al. In Vivo Light-Induced Activation of Neural Circuitry in Transgenic Mice Expressing Channelrhodopsin-2. *Neuron*. 2007;54(2):205–218.
33. Kleinlogel S, et al. Ultra light-sensitive and fast neuronal activation with the Ca<sup>2+</sup>-permeable channelrhodopsin CatCh. *Nat Neurosci*. 2011;14(4):513–518.
34. Zhou R, Abbas PJ, Assouline JG. Electrically evoked auditory brainstem response in peripherally myelin-deficient mice. *Hear Res*. 1995;88(1–2):98–106.
35. Bartels M, Hernandez VH, Krenkel M, Moser T, Salditt T. Phase contrast tomography of the mouse cochlea at microfocus x-ray sources. *Applied Physics Letters*. 2013;103(8):083703.
36. Müller M, von Hünnerbein K, Hoidis S, Smolders JWT. A physiological place-frequency map of the cochlea in the CBA/J mouse. *Hear Res*. 2005;202(1–2):63–73.
37. Stiebler I, Ehret G. Inferior colliculus of the house mouse. I. A quantitative study of tonotopic organization, frequency representation, and tone-threshold distribution. *J Comp Neurol*. 1985;238(1):65–76.
38. Snyder RL, Bierer JA, Middlebrooks JC. Topographic spread of inferior colliculus activation in response to acoustic and intracochlear electric stimulation. *J Assoc Res Otolaryngol*. 2004;5(3):305–322.
39. Willott JF. Effects of aging, hearing loss, and anatomical location on thresholds of inferior colliculus neurons in C57BL/6 and CBA mice. *J Neurophysiol*. 1986;56(2):391–408.
40. Noben-Trauth K, Zheng QY, Johnson KR. Association of cadherin 23 with polygenic inheritance and genetic modification of sensorineural hearing loss. *Nat Genet*. 2003;35(1):21–23.
41. Müller-Preuss P, Mitzdorf U. Functional anatomy of the inferior colliculus and the auditory cortex: current source density analyses of click-evoked potentials. *Hear Res*. 1984;16(2):133–142.
42. Mitzdorf U. Current source-density method and application in cat cerebral cortex: investigation of evoked potentials and EEG phenomena. *Physiol Rev*. 1985;65(1):37–100.
43. Harris DM. Current source density analysis of frequency coding in the inferior colliculus. *Hear Res*. 1987;25(2–3):257–266.
44. Happel MFK, Jeschke M, Ohl FW. Spectral integration in primary auditory cortex attributable to temporally precise convergence of thalamocortical and intracortical input. *J Neurosci*. 2010;30(33):11114–11127.
45. Sanes DH, Constantine-Paton M. The sharpening of frequency tuning curves requires patterned activity during development in the mouse, *Mus musculus*. *J Neurosci*. 1985;5(5):1152–1166.
46. Syka J, Popelář J, Kvasnák E, Astl J. Response properties of neurons in the central nucleus and external and dorsal cortices of the inferior colliculus in guinea pig. *Exp Brain Res*. 2000;133(2):254–266.
47. Palmer AR, Shackleton TM, Sumner CJ, Zobay O, Rees A. Classification of frequency response areas in the inferior colliculus reveals continua not discrete classes. *J Physiol (Lond)*. 2013;591(pt 16):4003–4025.
48. Izzo AD, et al. Laser stimulation of auditory neurons: effect of shorter pulse duration and penetration depth. *Biophys J*. 2008;94(8):3159–3166.
49. Strenzke N, et al. Complexin-I is required for high-fidelity transmission at the endbulb of held auditory synapse. *J Neurosci*. 2009;29(25):7991–8004.
50. Schwander M, et al. A forward genetics screen in mice identifies recessive deafness traits and reveals that pejavkin is essential for outer hair cell function. *J Neurosci*. 2007;27(9):2163–2175.
51. Pangršič T, et al. Hearing requires otoferlin-dependent efficient replenishment of synaptic vesicles in hair cells. *Nat Neurosci*. 2010;13(7):869–876.
52. Sewell WF. The effects of furosemide on the endocochlear potential and auditory-nerve fiber tuning curves in cats. *Hearing Res*. 1984;14(3):305–314.
53. Liu Y, et al. Protection against aminoglycoside-induced ototoxicity by regulated AAV vector-mediated GDNF gene transfer into the cochlea. *Mol Ther*. 2008;16(3):474–480.
54. Sheffield AM, et al. Viral vector tropism for supporting cells in the developing murine cochlea. *Hear Res*. 2011;277(1–2):28–36.
55. Praetorius M, et al. Transsynaptic delivery of nanoparticles to the central auditory nervous system. *Acta Otolaryngol*. 2007;127(5):486–490.
56. Staeker H, Li D, O'Malley BW Jr, Van De Water TR. Gene expression in the mammalian cochlea: a study of multiple vector systems. *Acta Otolaryngol*. 2001;121(2):157–163.
57. Lalwani AK, Walsh BJ, Reilly PG, Muzyczka N, Mhatre AN. Development of in vivo gene therapy for hearing disorders: introduction of adeno-associated virus into the cochlea of the guinea pig. *Gene Ther*. 1996;3(7):588–592.
58. Wareing M, et al. Cationic liposome mediated transgene expression in the guinea pig cochlea. *Hear Res*. 1999;128(1–2):61–69.
59. Wu J, Liu B, Fan J, Zhu Q, Wu J. Study of protective effect on rat cochlear spiral ganglion after blast exposure by adenovirus-mediated human  $\beta$ -nerve growth factor gene. *Am J Otolaryngol*. 2011;32(1):8–12.
60. Liu Y, et al. Specific and efficient transduction of



- Cochlear inner hair cells with recombinant adeno-associated virus type 3 vector. *Molecular Therapy*. 2005;12(4):725–733.
61. Bedrosian JC, et al. In vivo delivery of recombinant viruses to the fetal murine cochlea: transduction characteristics and long-term effects on auditory function. *Mol Ther*. 2006;14(3):328–335.
  62. Reisinger E, et al. Probing the functional equivalence of otoferlin and synaptotagmin 1 in exocytosis. *J Neurosci*. 2011;31(13):4886–4895.
  63. Brigande JV, Gubbels SP, Woessner DW, Jungwirth JJ, Breese CS. Electroporation-mediated gene transfer to the developing mouse inner ear. *Methods Mol Biol*. 2009;493:125–139.
  64. Taberner AM, Liberman MC. Response properties of single auditory nerve fibers in the mouse. *J Neurophysiol*. 2005;93(1):557–569.
  65. Oertel D. Use of brain slices in the study of the auditory system: spatial and temporal summation of synaptic inputs in cells in the anteroventral cochlear nucleus of the mouse. *J Acoust Soc Am*. 1985;78(1 pt 2):328–333.
  66. Shimano T, et al. Assessment of the AAV-mediated expression of channelrhodopsin-2 halorhodopsin in brainstem neurons mediating auditory signaling. *Brain Res*. 2013;1511:138–152.
  67. Miller CA, et al. Electrical excitation of the acoustically sensitive auditory nerve: single-fiber responses to electric pulse trains. *J Assoc Res Otolaryngol*. 2006;7(3):195–210.
  68. Gunaydin LA, et al. Ultrafast optogenetic control. *Nat Neurosci*. 2010;13(3):387–392.
  69. Diester I, et al. An optogenetic toolbox designed for primates. *Nature neuroscience*. 2011;14(3):387–397.
  70. Lignani G, et al. Long-term optical stimulation of channelrhodopsin-expressing neurons to study network plasticity. *Front Mol Neurosci*. 2013;6:22.
  71. Akil O, et al. Restoration of hearing in the VGLUT3 knockout mouse using virally mediated gene therapy. *Neuron*. 2012;75(2):283–293.
  72. Simonelli F, et al. Gene therapy for Leber's congenital amaurosis is safe and effective through 1.5 years after vector administration. *Mol Ther*. 2010;18(3):643–650.
  73. Willett K, Bennett J. Immunology of AAV-mediated gene transfer in the eye. *Front Immunol*. 2013;4:261.
  74. Mingozzi F, High KA. Immune responses to AAV vectors: overcoming barriers to successful gene therapy. *Blood*. 2013;122(1):23–36.
  75. Meyer AC, et al. Tuning of synapse number, structure and function in the cochlea. *Nat Neurosci*. 2009;12(4):444–453.
  76. Yan J, Ehret G. Corticofugal reorganization of the midbrain tonotopic map in mice. *Neuroreport*. 2001;12(15):3313–3316.
  77. Portfors CV, Mayko ZM, Jonson K, Cha GF, Roberts PD. Spatial organization of receptive fields in the auditory midbrain of awake mouse. *Neuroscience*. 2011;193:429–439.
  78. Mayo SC, et al. Quantitative X-ray projection microscopy: phase-contrast and multi-spectral imaging. *J Microsc*. 2002;207(pt 2):79–96.
  79. De Witte Y, Boone M, Vlassenbroeck J, Dierick M, Van Hoorebeke L, Bronnikov-aided correction for x-ray computed tomography. *J Opt Soc Am A Opt Image Sci Vis*. 2009;26(4):890–894.